

Tsunami modeling with dynamic seafloors: a high-order solver validated with shallow water benchmarks

Thomas Melkior^{a,b}, Harsha S. Bhat^b, Faisal Amlani^{a,*}

^a *Université Paris-Saclay, CentraleSupélec, ENS Paris-Saclay, CNRS, LMPS - Laboratoire de Mécanique Paris-Saclay, Gif-sur-Yvette, France*

^b *Laboratoire de Géologie, École Normale Supérieure, CNRS-UMR 8538, PSL Research University, 75006 Paris, France*

Abstract

Recent scientific studies have suggested that, in certain physical configurations, the time-dependent behavior of earthquake rupture and seafloor (bathymetry) motion can leave observable near-field signatures in tsunami wave generation and propagation. However, dynamic ground movement is often neglected in conventional tsunami models, which commonly assume instantaneous ground displacement (sourcing). This work introduces a pseudo-spectral algorithm for the solution of the nonlinear shallow water equations with time-dependent seafloor displacement and velocity. Based on a Fourier continuation (FC) methodology for the accurate trigonometric interpolation of a non-periodic function, the solver provides high-order convergence in space and time; mild (linear) Courant-Friedrichs-Lewy (CFL) constraints for explicit time integration; and results that are effectively free of numerical dispersion (or "pollution") errors. Such properties enable the efficient and robust resolution of the different space-time scales involved modeling tsunamis generated by dynamic earthquake ground motion (including over long distances). Numerical experiments attesting to accuracy and computational performance are presented with direct comparisons to high-order finite difference methodologies. The solver is physically validated by a number of classical and semi-classical benchmark cases based on simulated or experimental data. Additionally, a seismologically realistic, first-of-its-kind parametric study based on earthquake speed is introduced, whose results—easily facilitated by the FC-based approach proposed herein, with minimal numerical tuning—further demonstrate the potential importance of (and the motivation herein for) incorporating time-dependent seafloor behavior in quantitative tsunami hazard assessment.

Keywords: tsunami wave propagation, numerical analysis, shallow water equations, tsunami benchmarking, spectral methods, Fourier continuation

1. Introduction

The human and economic cost of tsunamis has been increasing in recent decades [1]. In order to better understand the underlying mechanisms of tsunami generation and propagation, numerical modeling has been indispensable, including for real-world events [2–4]. In particular, using physics-based simulations, it has been only recently shown [5, 6] that certain strike-slip earthquakes (which have minimal vertical displacement) can create significant waves, e.g., the deadly 2018 Palu bay, Indonesia tsunami [5] that was mysteriously and unexpectedly generated from such a fault (as opposed to from a classical tsunami-generating subduction zone,

*Corresponding author: faisal.amlani@ens-paris-saclay.fr

where the final, static, non-negligible vertical ground displacement is singularly important). This unusual tsunamigenesis was explained in a proof-of-concept work [5] by incorporating the time-dependent effects of so-called "supershear" earthquake rupture displacement and velocity into a simplified fluid-structure model. Such a finding has uncovered possible new risks (where there was thought to be little before) in a host of similar fault locations and configurations elsewhere [5], ultimately implying that there may be signatures yet to be discovered in fully dynamic considerations of seismogenic tsunami generation (including those by subduction zone/thrust fault ruptures). While others have also suggested the importance of considering dynamics in the near-field [4, 7], further study of this hypothesis requires fast, accurate, and robust numerical tools capable of more full-order, physically-faithful seismogenic tsunami modeling on realistic large-scale computational domains subjected to dynamic ground motion.

Conventionally, tsunami propagation is calculated at different scales: near-fields where the depth is low and where many strong nonlinearities can take place (e.g. wave breaking), and far-fields where the depth is high and some of these nonlinearities can be neglected [8]. Comprehensive tsunami solvers often use nested meshes where the choice of numerical method for each mesh depend on the scale [8]. At the near-field, methods able to treat can easily sharp gradients are better suited, such as the finite volume method [9, 10], the lattice Boltzmann method [11], or the smooth particle hydrodynamics (SPH) method [12, 13]. However, many of these methods can become costly for larger-scale configurations [8]. For long-distance and long-time tsunami wave propagation sourced by earthquakes, more computationally-efficient methods are often used, such as finite elements (FE) [14] or finite differences (FD) [8, 15, 16]. However, numerical dispersion or diffusion ("pollution") errors are well-known to be problematic for FD-based [17] or FE-based [18] solvers. For tsunami problems, this numerical pollution manifests as an accumulation of errors that grows as waves propagate further through space and time, eventually leading to considerable loss of accuracy. Consequently, such methods often require significant refinement that can quickly become prohibitively expensive in terms of computational cost for large-scale problems, potentially undermining their efficacy. Additionally, there are very few tsunami solvers in general that can consider time-dependent ground displacement and velocity induced by a rupture; those that can are often low-order accurate or too computationally expensive and sometimes only consider simple mathematical approximations to the full-order dynamic ground behavior [19, 20] (e.g., for black-box implementations). In order to fully incorporate dynamics, existing and commonly-used solvers require sometimes difficult or impractical modifications to the fundamental governing equations as well as their associated numerical methodologies: configurations involving such time-dependent sources (which can be of very high-frequency compared to the tsunami [5]) bring additional numerical and computational challenges in resolving all scales.

Hence the objective of this work is to introduce a new nonlinear shallow water equation (tsunami) solver based on a Fourier continuation (FC) approach for the trigonometric interpolation of non-periodic functions [21, 22]. Such an approach extends the applicability of Fourier series representations to general functions and boundary conditions while minimizing the well-known Gibbs "ringing effect" and enabling the use of the fast Fourier transform (FFT). FC has been employed successfully as a spectral method for solving various hyperbolic or parabolic partial differential equation (PDE) systems [21–31], achieving high accuracy by means of relatively coarse discretizations, a faithful preservation of the dispersion or diffusion characteristics of the underlying continuous operators (minimal numerical pollution errors), and mild (linear) CFL constraints on explicit time integration (properties that have facilitated applications to challenging scientific and engineering problems in both solid and fluid dynamics [5, 21, 29–32]). These features are well suited for resolving shallow

water equations since tsunami waves can propagate over long distances and long times. Additionally, such high-order capabilities are essential for the resolution of the different temporal scales that might be involved in modeling earthquake-induced tsunamis. Indeed, a particular novelty of the proposed solver is that it treats a more generalized or enriched version [7] of the classical shallow water equations in order to account for dynamic ground motion. Most conventional solvers employ static seafloor displacement, which is better suited for long wavelength far-field tsunami models [33, 34]; however, as described above, the dynamics of ground displacement and velocity may represent an important mechanism in some tsunamigenesis scenarios, particularly in the near-field [4–6].

Following an encouraging 1D proof-of-concept work on Palu [5], which demonstrates the potential of FC in addressing such challenges (the authors built a preliminary 1D solver for that specific case only), this contribution presents a general, full-fledged, high-order 1D and 2D tsunami solver that treats moving seafloors with high accuracy, FFT-speed, and minimal numerical pollution. The ultimate goal is to enable efficient simulations towards further parametric studies and explorations of the dynamic effects of earthquake ground motion on tsunamigenesis. After introducing the governing equations in Section 2, the solver based on FC is detailed in Section 3. Section 4 presents a comprehensive analysis of the numerical performance of the solver (attesting to high accuracy and efficiency), including comparisons to fourth- and sixth-order finite difference methods. Section 5 provide assessments of the solver on a number of realistic physical configurations that have been proposed extensively as benchmarks in literature (including comparisons to both experimental and simulated data). Section 6 presents the application of the FC-based solver to a newly-proposed parametric problem configuration with highly-dynamic seismic sources of different surface speeds, providing insight on the relevance of the new solver on scenarios that highlight the importance of time-dependent seafloor displacement. Concluding remarks are discussed in Section 7.

2. Governing equations

The high-order solver introduced in this work treats a physical model representing the behavior of tsunamis that is based on the shallow water equations (SWE) of Saint-Venant [35], which are a depth-averaged version of the Euler equations. The validity of these shallow water (tsunami) equations to model fluid flows rely on various principal hypotheses [36, 37]:

- The water depth $h(x, y, t)$ is small with respect to the wavelength of water waves.
- The fluid is incompressible.
- The flow is irrotational.
- The horizontal components of the velocity fields $u(x, y, t)$ (along x) and $v(x, y, t)$ (along y) are constant along the vertical component z .

In the present contribution, the system is treated in Cartesian coordinates—a valid approximation when propagation distances remain reasonable compared to the earth curvature [36, 37]. For larger-scale propagation, the system can be considered in spherical coordinates, for which the methodology introduced in this work can be straightforwardly extended.

The fundamental physical configuration is illustrated in Figure 1, where the total water depth $h(x, y, t)$ is decomposed as $h(x, y, t) = h_0(x, y) + \eta(x, y, t) - \xi(x, y, t)$ for given still water depth $h_0(x, y)$ corresponding to

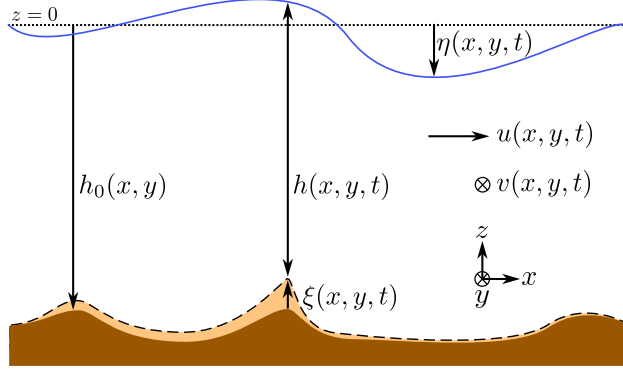


Figure 1: A representative illustration of the mathematical notations and physical definitions for the governing shallow water systems treated in this work.

a given unperturbed sea floor geometry (bathymetry) $h_0(x, y)$, a given ground motion vertical displacement $\xi(x, y, t)$ (the source), and unknown wave height $\eta(x, y, t)$ (i.e., displacement with respect to the at-rest free surface). The vertical displacement of the sea floor can be considered by different contributions [7], here, a first order approximation that neglects horizontal displacements is implemented. Commonly, ξ is enforced by an instantaneous water uplift [38] (i.e., an instantaneous free surface perturbation corresponding to $\eta(x, y, t = 0) = \max_t \xi(x, y, t)$). However, as discussed previously, the interest of this work is to develop a solver that can account for ground motion time history in order to model and study dynamic earthquake source effects (represented by displacement $\xi(x, y, t)$ and velocity $\xi_t(x, y, t)$ ¹) on tsunamigenesis. For the present work, the unperturbed sea depth $h_0(x, y)$ and the perturbation $\xi(x, y, t)$ (with its corresponding velocity $\xi_t(x, y, t)$) are given *a priori* (the latter possibly by separate rupture simulations or geophysical data [5, 6]).

Although the focus of the solver is 2D, the 1D equations are first introduced in what follows for facilitating the presentation and for completeness with respect to the 1D numerical experiments and benchmark cases that are discussed in Section 4 and Section 5. This work considers all systems in a classical nonlinear and nondispersive form, although the methodology can be easily extended to include additional terms such as those modeling friction, viscosity, and Coriolis effects.

2.1. 1D shallow water PDE system

In the 1D formulation of the SWE configuration shown in Figure 1, the transverse dimension y is considered invariant: the quantities do not depend on y and hence velocity in that direction is also neglected, i.e. $v = 0$. The corresponding 1D shallow water PDE system is given by [5]

$$\begin{cases} h_t + (hu)_x = 0, \\ (hu)_t + (hu^2)_x + gh\eta_x = 0, \end{cases} \quad (1)$$

where g is acceleration due to gravity (assumed to be 9.81 m/s^2 in this work unless indicated otherwise), where $h = h(x, t) = h_0(x) + \eta(x, t) - \xi(x, t)$, and where the unknowns are given by velocity $u = u(x, t)$ and free-surface displacement $\eta = \eta(x, t)$ for $x \in \Omega$ of spatial domain $\Omega \subset \mathbb{R}$, and a time interval $t \in [0, T]$

¹For compactness of notation, partial derivatives in x, y , and t are presented in subscript form throughout this work, e.g., $\partial \xi / \partial t(x, y, t) = \xi_t(x, y, t)$.

for $T \in \mathbb{R}^+$. The corresponding wave speed, $c = \sqrt{gh}$, can be approximated via a linearization of such equations [35–37]. Expanding, rearranging, and assuming $h > 0$ [39] yields the system given by

$$\begin{cases} \eta_t - \xi_t + (hu)_x = 0, \\ u_t + uu_x + g\eta_x = 0, \\ h(x, t) = h_0(x) + \eta(x, t) - \xi(x, t), \end{cases} \quad (2)$$

where the (given) perturbation of the sea floor $\xi(x, y, t)$ appears in both the h and h_t terms (again, such time-dependent ground motion is often neglected for tsunami modeling [5, 37]). In vectorial form, defining $\mathbf{U} = (\eta \ u)^T$, this can be written as

$$\mathbf{U}_t + \mathbf{F}(\mathbf{U}, \mathbf{U}_x) = \mathbf{S}, \quad (3)$$

where

$$\mathbf{F}(\mathbf{U}, \mathbf{U}_x) = \begin{pmatrix} (\eta_x + h_{0x} - \xi_x)u + (\eta + h_0 - \xi)u_x \\ uu_x + g\eta_x \end{pmatrix} \quad \text{and} \quad \mathbf{S} = \begin{pmatrix} \xi_t \\ 0 \end{pmatrix}.$$

The well-posedness of this system is completed by various Dirichlet, Neumann, or non-reflecting boundary conditions. The two classical boundary conditions for the shallow water system considered in this work are the so-called *wall boundary conditions* given by [40]

$$\begin{cases} \eta_x(x, t) = 0, \\ u(x, t) = 0, \end{cases} \quad x \in \partial\Omega, \quad t \in [0, T], \quad (4)$$

and the *radiation* (non-reflecting) boundary conditions given by [17]

$$\begin{cases} \eta_t(x, t) + c_n \eta_x(x, t) = 0, \\ u_t(x, t) + c_n u_x(x, t) = 0, \end{cases} \quad x \in \partial\Omega, \quad t \in [0, T], \quad (5)$$

where $c_n = \pm\sqrt{gh}$ is the propagation speed directed outward to the boundary at the right endpoint (i.e., $x = x_{\max}$) and left endpoint (i.e., $x = x_{\min}$), respectively.

2.2. 2D shallow water PDE system

The corresponding 2D SWE system (depth-averaged over the third dimension z) is given by [37, 41–43]

$$\begin{cases} \eta_t - \xi_t + (hu)_x + (hv)_y = 0, \\ u_t + uu_x + vu_y + g\eta_x = 0, \\ v_t + uv_x + vv_y + g\eta_y = 0, \\ h = h_0 + \eta - \xi, \end{cases} \quad (6)$$

where $u = u(x, y, t)$, $h_0 = h_0(x, y)$, $\eta = \eta(x, y, t)$ and $\xi = \xi(x, y, t)$ for $(x, y) \in \Omega$, $\Omega \subset \mathbb{R}^2$ being the considered spatial domain, and $t \in [0, T]$. In vectorial form, defining $\mathbf{U} = (\eta \ u \ v)^T$, this can be written, similarly to the 1D case above, as

$$\mathbf{U}_t + \mathbf{F}(\mathbf{U}, \nabla \mathbf{U}) = \mathbf{S}, \quad (7)$$

where

$$\mathbf{F}(\mathbf{U}, \nabla \mathbf{U}) = \begin{pmatrix} (\eta_x + h_{0,x} - \xi_x)u + (\eta + h_0 - \xi)u_x + (\eta_y + h_{0,y} - \xi_y)v + (\eta + h_0 - \xi)v_y \\ uu_x + vv_y + g\eta_x \\ uv_x + vv_y + g\eta_y \end{pmatrix} \quad \text{and} \quad \mathbf{S} = \begin{pmatrix} \xi_t \\ 0 \\ 0 \end{pmatrix}.$$

The corresponding 2D wall boundary conditions are given by [40]

$$\begin{cases} (\nabla \eta) \cdot \mathbf{n} = 0, \\ \mathbf{u} \cdot \mathbf{n} = 0, \end{cases} \quad (x, y) \in \partial\Omega, t \in [0, T], \quad (8)$$

where $\mathbf{u} = (u \ v)^T$ and \mathbf{n} is the normal outward to the boundary. The corresponding non-reflective (radiation) boundary conditions, assuming a propagation normal to the boundaries, are given by [17]

$$\begin{cases} \eta_t + c_n (\nabla \eta) \cdot \mathbf{n} = 0, \\ u_t + c_n (\nabla u) \cdot \mathbf{n} = 0, \\ v_t + c_n (\nabla v) \cdot \mathbf{n} = 0, \end{cases} \quad (x, y) \in \partial\Omega, \quad t \in [0, T], \quad (9)$$

where $c_n = \pm\sqrt{gh}$ is the propagation speed directed outward to the boundary (positive sign for right end, i.e. $x = x_{\max}$ or $y = y_{\max}$ boundaries).

3. A high-order SWE solver based on Fourier continuation (FC)

This section introduces a new, high-order, pseudo-spectral solver for treating both the 1D and 2D SWE systems described above. The methodology consists of employing a high-order Fourier continuation (FC) technique [21, 22] for trigonometric interpolation in space (and calculation of the subsequent derivatives in Equations (2) and (7)), together with an explicit high-order time integration scheme. The general principles of FC are presented in Section 3.1, and an accelerated version of this method is briefly described in Section 3.2. The complete solver is summarized in Section 3.3.

3.1. Spatial discretization

Let $N \in \mathbb{N}^*$ represent the number of points discretizing a smooth (possibly non-periodic) function $f : [0, 1] \rightarrow \mathbb{R}$. Here, the unit interval is considered without loss of generality (but can be applied to any interval by simple affine transformation, as is the case for all results of this paper). Defining $\{x_j\}$ as the grid points corresponding to a uniform discretization of the domain $[0, 1]$, i.e., $x_j = j\Delta x$, $0 \leq j \leq N-1$ where $\Delta x = 1/(N-1)$, the FC method consists of extending f into a function f^c that is periodic on a slightly larger interval $[0, b]$, $b > 1$ and that is given by a band-limited trigonometric (Fourier) series as

$$f^c : \begin{cases} [0, b] \rightarrow \mathbb{C} \\ x \mapsto \sum_{k=-M}^M a_k \exp\left(\frac{2\pi i k x}{b}\right), \end{cases} \quad (10)$$

where $M = (N+C)/2$ (for a number of C extension points that define the interval b , i.e., $b = (N+C-1)\Delta x$). The coefficients $\{a_k\}$, $k = -M, \dots, M$ are determined by minimizing the discrete error between f^c and the

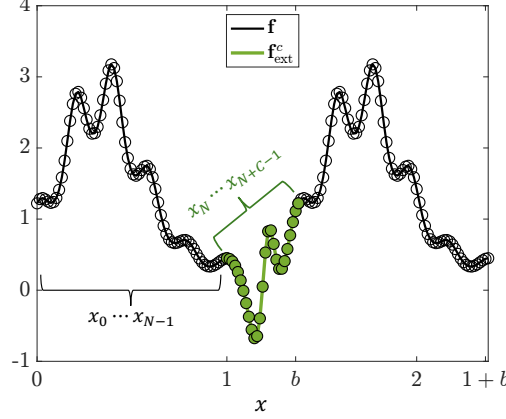


Figure 2: A representative illustration of a periodic extension produced by Fourier continuation.

original function f evaluated at the grid points $\mathbf{x} = (x_0 \dots x_{N-1})^T$, i.e.,

$$\{a_k\} = \arg \min \|f^c(\mathbf{x}) - f(\mathbf{x})\|_2. \quad (11)$$

In other words, f^c approximates a trigonometric interpolation of f on its discrete points. Figure 2 illustrates the corresponding extension that is achieved for an original discretized function $\mathbf{f} = (f(x_0) \dots f(x_{N-1}))^T$, where $\mathbf{f}_{\text{ext}}^c$ represents the C interpolated values in $[1, b]$. The complete discrete continuation function \mathbf{f}^c is given discretely by

$$\mathbf{f}^c = (\mathbf{f} \ \mathbf{f}_{\text{ext}}^c)^T = (f(x_0), \dots, f(x_{N-1}), f_{\text{ext}}^c(x_N), \dots, f_{\text{ext}}^c(x_{N+C-1}))^T.$$

Once the coefficients of the Fourier series expansion f^c in Eq. (10) have been determined, its corresponding spatial derivatives can be obtained analytically by term-wise differentiation, i.e.,

$$(f^c)'(x) = \sum_{k=-M}^M \frac{2\pi i k}{b} a_k \exp\left(\frac{2\pi i k x}{b}\right). \quad (12)$$

Thus, one obtains an approximation of the derivative of f by restricting f^c to the original interval, i.e.,

$$f'(x) \approx (f^c)'(x) \quad \forall x \in [0, 1]. \quad (13)$$

As in other spectral approaches, if f is infinitely differentiable (C^∞), the truncation error of such an approximation converges to zero faster than any finite power of Δx [17].

In practice, for a time-domain PDE solver, such extensions needs to be constructed at each timestep ($\{a_k\}$ changes at each timestep). That is, Eq. (11) must be solved, for example using a Singular Value Decomposition (SVD), at each timestep. The corresponding computational complexity of such minimizations is well-known to be $\mathcal{O}(N^3)$, which is too computationally expensive for dynamic problems where the SVD must be applied at each timestep. For this, an accelerated method known as FC(Gram) is employed in the solver proposed in this work (detailed in the following section).

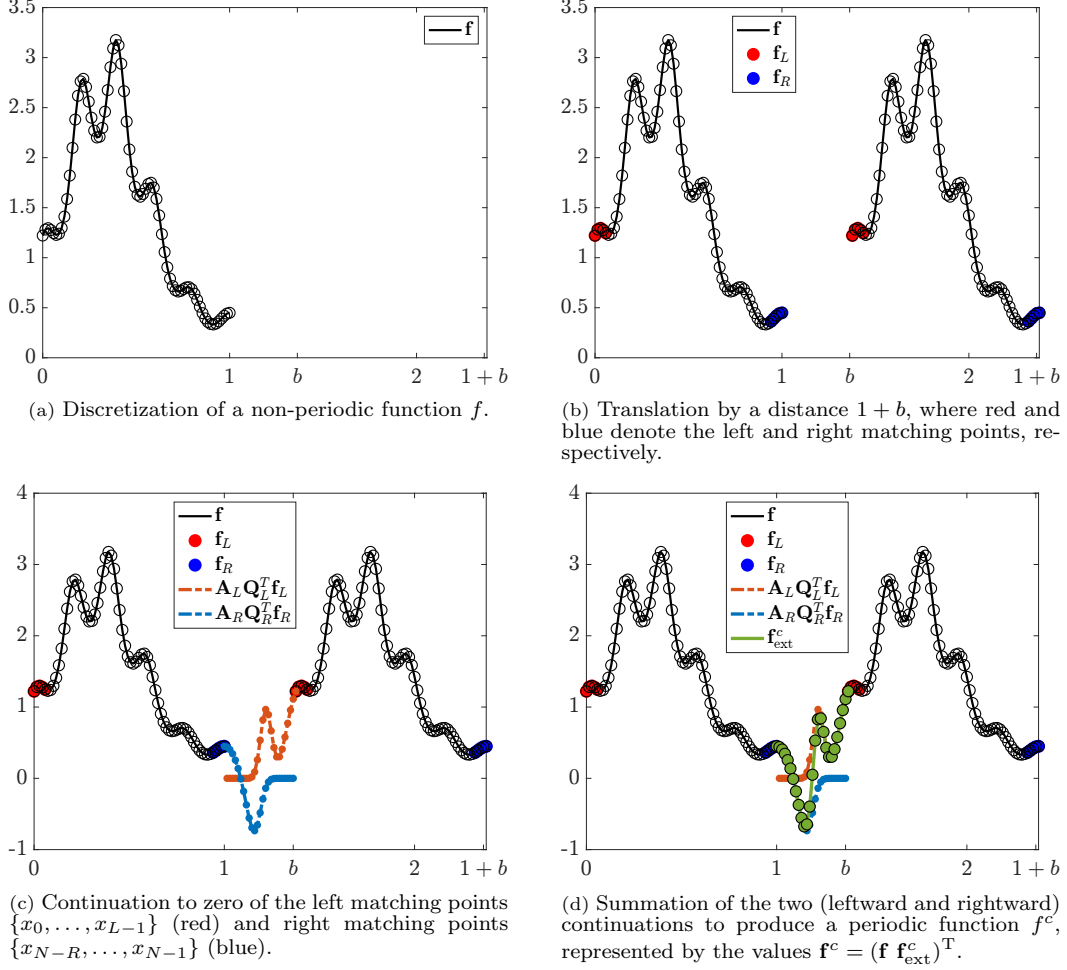


Figure 3: A summary of the accelerated FC(Gram) continuation methodology.

3.2. Accelerated Fourier continuation: FC(Gram)

An accelerated version of FC has been developed in order to pre-calculate extensions to enable its use with reasonable computational cost while maintaining its interesting properties (high order of accuracy, minimal numerical dispersion) [21–23, 28]. This accelerated version is referred as FC(Gram) because it involves Gram polynomials on which a continuation *basis* is precomputed and on which a handful of left and right endpoint function values are projected to form the complete continuation. A visualization of the accelerated continuation procedure, which is detailed in what follows, is presented in Figure 3.

Define two subsets of points on the left and right ends of $\{x_0, \dots, x_{N-1}\}$ (see Figure 3b): $\{x_0, \dots, x_{L-1}\}$ (where $L \in \mathbb{N}^*$ is the number of left points, $L \leq N$) and $\{x_{N-R}, \dots, x_{N-1}\}$ (where $R \in \mathbb{N}^*$ is the number of right points). These points are referred to as *matching points* in this work because each of these two subsets of points will be interpolated by a polynomial and used to continue the original discrete function. The continuation is done separately for each sides, enabling more flexibility in the choice of number of matching points as well as particular boundary conditions.

On the left side, there exists a polynomial of degree $L - 1$ that considers discrete function values $\{f(x_0), \dots, f(x_{L-1})\}$ at the corresponding matching points $\{x_0, \dots, x_{L-1}\}$ (additionally, this polynomial is

unique). Finding the corresponding coefficients c_0, \dots, c_{L-1} of an interpolating polynomial is given by the system

$$\begin{cases} c_0 + c_1 x_0 + c_2 (x_0)^2 \cdots + c_{L-1} (x_0)^{L-1} = f(x_0), \\ \vdots \\ c_0 + c_1 x_{L-1} + c_2 (x_{L-1})^2 + \cdots + c_{L-1} (x_{L-1})^{L-1} = f(x_{L-1}), \end{cases} \quad (14)$$

which can equivalently be written in matrix form as

$$\mathbf{P}_L \mathbf{c}_L = \mathbf{f}_L,$$

where

$$\mathbf{P}_L = \begin{pmatrix} 1 & x_0 & (x_0)^2 & \cdots & (x_0)^{L-1} \\ \vdots & \vdots & \vdots & & \vdots \\ 1 & x_{L-1} & (x_{L-1})^2 & \cdots & (x_{L-1})^{L-1} \end{pmatrix}, \quad \mathbf{c}_L = \begin{pmatrix} c_0 \\ \vdots \\ c_{L-1} \end{pmatrix}, \quad \text{and} \quad \mathbf{f}_L = \begin{pmatrix} f(x_0) \\ \vdots \\ f(x_{L-1}) \end{pmatrix}. \quad (15)$$

By employing a modified Gram-Schmidt orthonormalization, the real-valued square matrix \mathbf{P}_L (also known as a *Vandermonde matrix*) can be decomposed as $\mathbf{P}_L = \mathbf{Q}_L \mathbf{R}_L$, where \mathbf{Q}_L is an orthogonal matrix ($\mathbf{Q}_L \mathbf{Q}_L^T = \mathbf{I}_L$, the identity matrix of order L) and \mathbf{R}_L is an upper triangular matrix. The columns of \mathbf{Q}_L form an orthonormal basis of polynomials. The strategy of FC(Gram) consists in performing the continuation on this basis of polynomials (each column of the corresponding \mathbf{Q}_L), before projecting the matching points onto such basis. This enables one to invoke the SVD-based procedure that form continuations independently of the specific values of the matching points \mathbf{f}_L (which may evolve in time). That is, the extensions are pre-computed as a basis *a priori*. A similar procedure can then be performed for the rightward matching points to construct another basis of polynomials forming the columns of a matrix \mathbf{Q}_R .

With the orthonormalized Gram basis in hand, the first step of the FC(Gram) procedure is to build operators \mathbf{A}_L and \mathbf{A}_R that continue \mathbf{Q}_L and \mathbf{Q}_R to zero (i.e., leftwardly and rightwardly), so that their sum gives a global continuation that smoothly connects the left and right sides of f . For example, to continue \mathbf{Q}_L to zero, one takes its column vectors \mathbf{q}_L^j , which contain the L values $q_{j,L}(x_0), q_{j,L}(x_1), \dots, q_{j,L}(x_{L-1})$, and searches for an auxiliary interpolating trigonometric polynomial of the form given by [21]

$$q_{j,L}^c : \begin{cases} [0, (L + 2C + Z) \Delta x] \rightarrow \mathbb{C} \\ x \mapsto \sum_{k=-M}^M a_{k,j} \exp\left(\frac{2\pi i k x}{(L + 2C + Z - 1) \Delta x}\right), \end{cases} \quad (16)$$

where Z is a number of points equal to zero to match for blending and where $\{a_{k,j}\}$ are the unknown coefficients. The role of $q_{j,L}^c$ is to:

- approximate the $q_{j,L}$ values in $[0, (L - 1) \Delta x]$;
- smoothly continue (or “blend”) over C points the $q_{j,L}$ values to zero in $[L \Delta x, (L + C - 1) \Delta x]$;
- smoothly approximate the Z zero-valued points in $[(L + C) \Delta x, (L + C + Z - 1) \Delta x]$ that force the continuation to zero;
- smoothly continue the zero values over a certain number of extra points (here, taken to be C) in $[(L + C + Z) \Delta x, (L + 2C + Z - 1) \Delta x]$ to obtain periodicity over the auxiliary interval.

The coefficients $a_{k,j}$ satisfying the above can be found by solving an L^2 minimization problem, i.e.,

$$(a_{k,j})_k = \arg \min \left\| q_{j,L}^c(\mathbf{x}'_L) - \begin{pmatrix} q_{j,L}(\mathbf{x}_L) \\ \mathbf{0}_{Z \times 1} \end{pmatrix} \right\|_2, \quad (17)$$

where $\mathbf{x}_L = (x_0 \dots x_{L-1})^T$, $\mathbf{x}'_L = (x_0 \dots x_{L+Z-1})^T$ and $\mathbf{0}_{Z \times 1}$ is a zero vector of length Z . The solution defined by Eq. (17) can be obtained for each of the j base polynomials $q_{j,L}$ via a truncated SVD. The resulting periodic continuation operator for \mathbf{Q}_L formed by the $(q_{j,L}^c)_j$ is hence given by

$$(\mathbf{A}_L)_{m,j} = q_{j,L}^c(x_{m-1}), \quad m \in \{1, \dots, L+C\}, \quad j \in \{1, \dots, L\}. \quad (18)$$

Such a continuation operator is clearly pre-computed since the minimization problem does not depend on the specific function values of f (merely the interpolating basis). In a similar manner to all of the above, one can straightforwardly construct an operator \mathbf{A}_R that continues \mathbf{f}_R to zero rightwardly with R matching points.

Remark 3.1. For equal left and right matching points (i.e., $L = R$), the corresponding FC operators $\mathbf{Q}_L, \mathbf{Q}_R$ (respectively $\mathbf{A}_L, \mathbf{A}_R$) differ only by column-wise ordering (respectively row-wise). Hence the precomputation of such operators needs only to be conducted on one side.

The second step of the FC(Gram) procedure is to project the left and right endpoints \mathbf{f}_L and \mathbf{f}_R by

$$\begin{cases} \text{proj}(\mathbf{f}_L) = \mathbf{Q}_L^T \mathbf{f}_L, \\ \text{proj}(\mathbf{f}_R) = \mathbf{Q}_R^T \mathbf{f}_R, \end{cases} \quad (19)$$

to get the corresponding coefficients in the continuation basis \mathbf{A}_L and \mathbf{A}_R , respectively. Hence, the quantity $\mathbf{A}_L \mathbf{Q}_L^T \mathbf{f}_L$ represents the leftward continuation of the left values \mathbf{f}_L towards zero and, similarly, the quantity $\mathbf{A}_R \mathbf{Q}_R^T \mathbf{f}_R$ represents the rightward continuation of the right values \mathbf{f}_R towards zero (see Figure 3c). In the end, the sum $\mathbf{A}_L \mathbf{Q}_L^T \mathbf{f}_L + \mathbf{A}_R \mathbf{Q}_R^T \mathbf{f}_R$ represents the complete continuation that matches the left end of the original discrete function \mathbf{f} with the right over an interval of C points (Figure 3d). Hence the final discrete continued function \mathbf{f}^c is given by

$$\mathbf{f}^c = \begin{pmatrix} \mathbf{f} \\ \mathbf{A}_L \mathbf{Q}_L^T \mathbf{f}_L + \mathbf{A}_R \mathbf{Q}_R^T \mathbf{f}_R \end{pmatrix}, \quad (20)$$

which matches f discretely on the original interval $[0, 1]$, but is periodic on a slightly larger interval $[0, b]$ (discretely, $b = (N+C-1)\Delta x$). Hence the vector \mathbf{f}^c represents discrete values of a corresponding continuous periodic function f^c .

Thanks to this acquired periodicity, one can now approximate f^c by the truncated Fourier series

$$x \mapsto \sum_{k=-M}^M \alpha_k \exp\left(\frac{2\pi i k x}{b}\right),$$

where the coefficients $\{\alpha_k\}$ can be obtained directly using the Fast Fourier Transform (FFT) [44] of the function's corresponding discretization \mathbf{f}^c , i.e., $\hat{\mathbf{f}}^c = \text{fft}(\mathbf{f}^c) = (\alpha_{-M/2} \dots \alpha_{M/2})^T$. The discrete derivative can finally be obtained by forming the coefficients of the term-wise differentiation of the series (see Eq. (12)) and performing the inverse (Fast) Fourier transform given by

$$\mathbf{f}' \approx (\mathbf{f}^c)' \approx \text{ifft}(\mathbf{K} \hat{\mathbf{f}}^c), \quad (21)$$

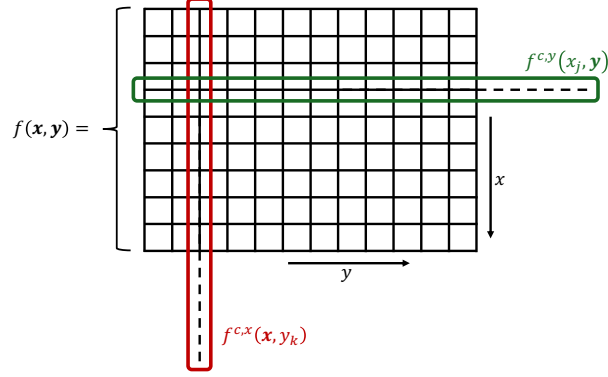


Figure 4: A representative illustration of a 2D "slice-wise" Fourier continuation.

where \mathbf{K} is a matrix containing identical column vectors whose k -th component is $2\pi i \alpha_k k/b$. The overall algorithm described above incurs significantly less computational cost than the simplest FC described in Section 3.1 which requires an SVD each time an extension needs to be produced. Indeed, the $\mathcal{O}(N^3)$ continuation is only done once for the Gram polynomials in the accelerated version, after which it is stored. Once these pre-computed operators have been loaded, the resulting PDE resolution in space is dominated by the FFT, whose complexity is $\mathcal{O}(N \log N)$ [44].

Remark 3.2. *The complete FC(Gram) algorithm employed in the present solver uses a number of extra zero points for the continuation, as well as an oversampling of values in order to mitigate the numerical ill-conditioning well-known for Vandermonde matrices. Additionally, the overall precomputation procedure uses symbolic algebra for the QR decompositions and high-precision arithmetic for the SVDs (256 digits instead of 16 for a double). For simplicity and clarify of the above presentations, these details are left to the reader [21].*

3.2.1. Extension to higher spatial dimensions

Consider a discretization of $(N_x, N_y) \in (\mathbb{N}^*)^2$ points for a smooth function $f : [0, 1]^2 \rightarrow \mathbb{R}$, i.e., $x_j = j\Delta x$, $0 \leq j \leq (N_x - 1)$ for $\Delta x = 1/(N_x - 1)$ and $y_k = k\Delta y$, $0 \leq k \leq (N_y - 1)$ for $\Delta y = 1/(N_y - 1)$. The accelerated FC(Gram) can be extended to 2D problem line-wise. The discrete values of f , now represented by a matrix $\mathbf{f} \in \mathbb{R}^{N_x \times N_y}$, can be considered as a set of 1D slices on which to apply the FC procedure. Thus, two extensions are obtained: $f^{c,x}$, representing the continued function with respect to x for each y -slice, and $f^{c,y}$, representing the continued function with respect to y for each x -slice. These functions can be discretely represented at the points (x_j, y_k) by the matrices $\mathbf{f}^{c,x}$ and $\mathbf{f}^{c,y}$, respectively. This procedure is not a proper 2D continuation, but a "2D slice-wise" continuation. The Figure 4 illustrates this method of application of the 1D FC(Gram) procedure over the 2D grid. Once the continuations are properly constructed, one can differentiate slice by slice the x and y continuations, just as before:

$$\frac{\partial f}{\partial x} \approx \frac{\partial f^{c,x}}{\partial x} \quad \text{and} \quad \frac{\partial f}{\partial y} \approx \frac{\partial f^{c,y}}{\partial y}. \quad (22)$$

Remark 3.3. *In the rest of this manuscript, and particularly in the results, 'FC' refers to the accelerated FC(Gram) methodology.*

3.3. Time integration

The full shallow water PDE solver developed herein exploits the precision of FC in its accelerated version. The FC(Gram) method that enables high-order computation of the spatial derivatives, is completed with

a time integration scheme in order to build a complete PDE solver. Classical integration methods are applicable, including the forward Euler method. However, to remain consistent with the high-order and dispersionless properties of FC, which are needed to model earthquake-generated tsunamis, a suitably high-order time scheme is employed in the solver introduced in this work. Although the well-known fourth-order Runge-Kutta (RK4) scheme is a common choice, in the interest of computational speed, a more convenient choice is fourth-order Adams-Bashforth (AB4), whose regions of stability are still adequate [45], including for FC-based methods [21, 30]. An obvious advantage of using the AB4 of Eq. (25) instead of the RK4 of Eq. (26) is that the latter can be slow in the current multi-dimensional PDE context since it relies on calculating three intermediate time stages for each timestep update, leading to four evaluations per timestep of the right-hand side (whose cost is dominated by the FC procedure). On the other hand, AB4 requires only one calculation of the right-hand side per timestep (at the lower cost of stocking the previous three right-hand sides). Additionally, at the same timestep, AB4 and RK4 have been shown to have equivalent accuracy in other FC-based solvers [29].

After spatial discretization and differentiation, the corresponding ordinary differential equations (ODEs) in time are of the form

$$\mathbf{U}'(t) = \mathbf{RHS}(t, \mathbf{U}(t)), \quad (23)$$

where $\mathbf{U}(t) = (\boldsymbol{\eta}(t) \mathbf{u}(t) \mathbf{v}(t))^T$, $\boldsymbol{\eta}(t) = \{\eta(x_j, y_k, t)\}$, and the corresponding right-hand side (Eq. (7)) given by

$$\mathbf{RHS}(t, \mathbf{U}(t)) = -\mathbf{F}(\mathbf{U}(t), \nabla \mathbf{U}(t)) + \mathbf{S}(t). \quad (24)$$

Employing AB4 [45], the resulting discrete formulation for evolving to a timestep $n + 1$ (corresponding to time t^{n+1}) is given by

$$\mathbf{U}^{n+1} = \mathbf{U}^n + \frac{\Delta t}{24} [55\mathbf{RHS}(t^n, \mathbf{U}^n) - 59\mathbf{RHS}(t^{n-1}, \mathbf{U}^{n-1}) + 37\mathbf{RHS}(t^{n-2}, \mathbf{U}^{n-2}) - 9\mathbf{RHS}(t^{n-3}, \mathbf{U}^{n-3})]. \quad (25)$$

The computation of \mathbf{RHS} involves determining the spatial derivatives, which is accomplished using the 2D-slicewise FC(Gram) method described in Section 3.2. The corresponding procedure for computing \mathbf{RHS} is summarized in Algorithm 1.

Algorithm 1: Computation of the right-hand side for time integration.

Input: vector of discrete unknowns \mathbf{U} , the current timestep t , and a given dynamic sea floor motion $\boldsymbol{\xi}$ with derivatives $\boldsymbol{\xi}_x, \boldsymbol{\xi}_y, \boldsymbol{\xi}_t$

Output: right-hand side \mathbf{RHS}

Function $\mathbf{RHS}(t, \mathbf{U}, \boldsymbol{\xi}, \boldsymbol{\xi}_x, \boldsymbol{\xi}_y, \boldsymbol{\xi}_t)$:

$\mathbf{U}_x \leftarrow \text{FC_deriv_x}(\mathbf{U})$ $\mathbf{U}_y \leftarrow \text{FC_deriv_y}(\mathbf{U})$ $\mathbf{h} \leftarrow \mathbf{h}_0 + \boldsymbol{\eta} - \boldsymbol{\xi}$ $\mathbf{h}_x \leftarrow \mathbf{h}_{0x} + \boldsymbol{\eta}_x - \boldsymbol{\xi}_x$ $\mathbf{h}_y \leftarrow \mathbf{h}_{0y} + \boldsymbol{\eta}_y - \boldsymbol{\xi}_y$ $\mathbf{RHS} \leftarrow - \begin{pmatrix} \mathbf{h}_x \mathbf{u} + \mathbf{h}_y \mathbf{v} + \mathbf{h}_t \mathbf{w} \\ \mathbf{u} \mathbf{u}_x + \mathbf{v} \mathbf{u}_y + g \boldsymbol{\eta}_x \\ \mathbf{u} \mathbf{v}_x + \mathbf{v} \mathbf{v}_y + g \boldsymbol{\eta}_y \end{pmatrix} + \begin{pmatrix} \boldsymbol{\xi}_t \\ \mathbf{0} \\ \mathbf{0} \end{pmatrix}$	$// \mathbf{U}_x = (\boldsymbol{\eta}_x \mathbf{u}_x \mathbf{v}_x)^T \text{ via Section 3.2}$ $// \mathbf{U}_y = (\boldsymbol{\eta}_y \mathbf{u}_y \mathbf{v}_y)^T \text{ via Section 3.2}$
---	--

return

Remark 3.4. Since the use of AB4 requires knowledge of three previous timesteps, the proposed SWE solver is initialized by computing the first three iterations (timesteps) via RK4 via the time evolution expression

given by

$$\mathbf{U}^{n+1} = \mathbf{U}^n + \frac{\Delta t}{6} (\mathbf{k}_1 + 2\mathbf{k}_2 + 2\mathbf{k}_3 + \mathbf{k}_4), \quad (26)$$

where

$$\begin{cases} \mathbf{k}_1 = \text{RHS}(t^n, \mathbf{U}^n), \\ \mathbf{k}_2 = \text{RHS}\left(t^n + \frac{\Delta t}{2}, \mathbf{U}^n + \frac{\Delta t}{2} \mathbf{k}_1\right), \\ \mathbf{k}_3 = \text{RHS}\left(t^n + \frac{\Delta t}{2}, \mathbf{U}^n + \frac{\Delta t}{2} \mathbf{k}_2\right), \\ \mathbf{k}_4 = \text{RHS}(t^n + \Delta t, \mathbf{U}^n + \Delta t \mathbf{k}_3). \end{cases}$$

Alternatively, one could simply start the simulation after three ‘zero-state’ iterations, which is acceptable for a number of realistic problems that may begin at rest.

3.4. Implementation details & solver summary

The resulting overall solver is summarized in [Algorithm 2](#), where the selection and application of the boundary conditions are indicated by the function `ApplyBC`, which considers walls ([Eq. \(8\)](#)), radiation boundary conditions ([Eq. \(9\)](#)), or prescribed (Dirichlet) values. FC-based solutions in this work are obtained in MATLAB 2023b Update 6 employing a self-developed code. Similarly, the FD-based solvers employed for comparison utilize fully self-implemented code in MATLAB. All results herein are obtained from computations performed on the same MacBook Air M2 2022 with 16GB of RAM.

For the simulations and studies that follow, the number of matching points is taken to be $L = R = 5$ and the number of continuation points is taken to be $C = 25$. Additionally, as is the case for classical spectral methods [\[46\]](#) as well as FC-based methods [\[21, 29, 30\]](#), a filter σ is used in the context of time-domain PDEs such that the n -th component of the discrete Fourier coefficients is appropriately scaled for stability, i.e., $2\pi\sigma(\alpha_n)in/b$, where $\sigma(n) = \exp(-\alpha(n/M)^{2p})$ for $\alpha = 16c\Delta t \log(10^{-2})/\Delta x$, $p = 4$, approximate wave speed $c \approx \sqrt{gH}$ (where H is the mean or still water depth), M as defined in [Section 3.1](#), and the frequency index n (such that $-M \leq n \leq M$). Unless otherwise stated, the timestep chosen for all simulations in this work is determined from the CFL condition given by $\Delta t = \text{CFL} \Delta x/c$ in 1D and $\Delta t = \text{CFL} \min(\Delta x, \Delta y)/c$ in 2D, with corresponding CFL constants given in 1D for the FC solver as well as reference fourth- and sixth-order finite differences (FD4 and FD6, respectively) by $\text{CFL}_{1D}^{\text{FC}} = 0.17$, $\text{CFL}_{1D}^{\text{FD4}} = 0.21$, $\text{CFL}_{1D}^{\text{FD6}} = 0.18$, respectively, and for 2D by $\text{CFL}_{2D}^{\text{FC}} = 0.1$, $\text{CFL}_{2D}^{\text{FD4}} = 0.17$, $\text{CFL}_{2D}^{\text{FD6}} = 0.14$, respectively. The values of these constants have been empirically determined to be the largest such values that ensure stability, where FC carries slightly smaller (but similar) CFL constants to the FD-based schemes considered for comparison in [Section 4](#).

Remark 3.5. *The complexity of the 1D solver scales as $\mathcal{O}(N_t N \log(N))$ (since the additional C continuation points are fixed), where N_t is the number of timesteps, and N the number of 1D spatial discretization points. In 2D, the corresponding complexity is $\mathcal{O}(N_t N_x N_y \log(N_{\max}))$, where N_x, N_y are the number of spatial discretization points in the two directions, and $N_{\max} = \max(N_x, N_y)$. An important remark on this result is that the ratio of complexity between FC and finite differences is only $\log(N_{\max})$, i.e., FC is only a factor $\log(N_{\max})$ more costly than FD. This is an acceptable compromise for the high-order convergence and numerically dispersionless behavior of an FC solver that is demonstrated in [Section 4](#), which ultimately results in simulations that are cheaper than FD (to achieve the same error) for realistic settings, especially those including long-distance or long-time propagation.*

Algorithm 2: A summary of the FC-based solver for shallow water systems.

Input: $\eta^1 = \eta(\mathbf{x}, \mathbf{y}, t = 0)$, $\mathbf{u}^1 = u(\mathbf{x}, \mathbf{y}, t = 0)$, $\mathbf{v}^1 = v(\mathbf{x}, \mathbf{y}, t = 0)$, Δt , N_t , ξ , ξ_x , ξ_y , ξ_t
Output: $\eta^n, \mathbf{u}^n, \mathbf{v}^n, \forall n \in \{1, \dots, N_t\}$ (complete space-time solutions)

$\mathbf{U}^1 \leftarrow (\eta^1, \mathbf{u}^1, \mathbf{v}^1)^\top$ // Initial values

for $n = 1, \dots, 3$ // Initialize first three timesteps via RK4
do
 $\mathbf{k}_1 \leftarrow \text{RHS}(t^n, \mathbf{U}^n, \xi, \xi_x, \xi_y, \xi_t)$
 $\mathbf{k}_2 \leftarrow \text{RHS}\left(t^n + \frac{\Delta t}{2}, \mathbf{U}^n + \frac{\Delta t}{2} \mathbf{k}_1, \xi, \xi_x, \xi_y, \xi_t\right)$
 $\mathbf{k}_3 \leftarrow \text{RHS}\left(t^n + \frac{\Delta t}{2}, \mathbf{U}^n + \frac{\Delta t}{2} \mathbf{k}_2, \xi, \xi_x, \xi_y, \xi_t\right)$
 $\mathbf{k}_4 \leftarrow \text{RHS}(t^n + \Delta t, \mathbf{U}^n + \Delta t \mathbf{k}_3, \xi, \xi_x, \xi_y, \xi_t)$
 $\mathbf{U}^{n+1} = \mathbf{U}^n + \frac{\Delta t}{6} (\mathbf{k}_1 + 2\mathbf{k}_2 + 2\mathbf{k}_3 + \mathbf{k}_4, \xi, \xi_x, \xi_y, \xi_t)$
 $\mathbf{U}^{n+1} \leftarrow \text{ApplyBC}(t^{n+1}, \mathbf{U}^{n+1})$ // Boundary conditions
end
 $\text{RHS}^{n-2} \leftarrow \text{RHS}(t^1, \mathbf{U}^1, \xi, \xi_x, \xi_y, \xi_t)$
 $\text{RHS}^{n-1} \leftarrow \text{RHS}(t^2, \mathbf{U}^2, \xi, \xi_x, \xi_y, \xi_t)$
 $\text{RHS}^n \leftarrow \text{RHS}(t^3, \mathbf{U}^3, \xi, \xi_x, \xi_y, \xi_t)$

for $n = 4, \dots, N_t$ // Main loop (AB4)
do
 $\text{RHS}^{n-3} \leftarrow \text{RHS}^{n-2}$
 $\text{RHS}^{n-2} \leftarrow \text{RHS}^{n-1}$
 $\text{RHS}^{n-1} \leftarrow \text{RHS}^n$
 $\text{RHS}^n \leftarrow \text{RHS}(t^n, \mathbf{U}^n, \xi, \xi_x, \xi_y, \xi_t)$
 $\mathbf{U}^{n+1} = \mathbf{U}^n + \frac{\Delta t}{24} (55\text{RHS}^n - 59\text{RHS}^{n-1} + 37\text{RHS}^{n-2} - 9\text{RHS}^{n-3})$
 $\mathbf{U}^{n+1} \leftarrow \text{ApplyBC}(t^{n+1}, \mathbf{U}^{n+1})$
end

4. Numerical performance of the solver

The objective of this section is to verify accuracy, convergence, and code implementation of the FC SWE solver introduced in this work (including via comparisons with standard high-order finite difference methods). The classical method of manufactured solutions [21, 29, 47] is employed throughout this section, allowing one to impose any given analytical function as a solution to the PDE of interest by prescribing a non-trivial right-hand-side forcing/source term (determined via substitution of the postulated solution into the PDE) and choosing appropriate initial values and boundary conditions. Such an approach enables the error of a methodology to be determined accurately and its solver implementation to be verified numerically. For the results that follow in this section, the solver detailed in Section 3 is assessed against self-implemented finite difference solvers employing exactly the same temporal integration techniques (RK4+AB4), i.e., differing only by spatial differentiation. The FD solvers considered here employ central difference schemes of order four and six, where boundary derivatives are calculated via ghost points [48].

4.1. Convergence experiments

In order to assess convergence, the following manufactured reference solution over a 1D spatial domain $[0, 1]$ is considered, which contains complex variations in time and space:

$$\begin{cases} \eta(x, t) = \sin(5x - 3t) \sin(23x - 5t), \\ u(x, t) = \cos(2.5x - t) \cos(17x - 4t). \end{cases} \quad (27)$$

Since a principal objective of the SWE methodology introduced in this work is to treat highly dynamic sea-floor movement, a corresponding time-dependent (coseismic) displacement ξ is additionally considered:

$$\xi(x, t) = \sin(53x - 13t) \sin(3x - 15t). \quad (28)$$

The coefficients employed for ξ have been intentionally chosen to be of higher frequency in both space and time than either η or u , inspired by seismogenic configurations where earthquake dynamics are significantly faster than the corresponding water waves. With an additional consideration of a flat bathymetric (unperturbed) profile given by $h_0(x) = 5$, the total $h(x, t) = \eta(x, t) + h_0(x) - \xi(x, t)$ remains positive at all times t . Snapshots of the manufactured η , u and ξ given above are presented in [Figure 5](#), overlaid with the corresponding discrete representation that is produced by the coarsest discretization considered.

Simulations are performed employing $g = 1$ in the shallow water equations for a series of increasing spatial resolutions of $\Delta x = 0.02, 0.01, 0.005, 0.00025, 0.000125$. All simulations are advanced to a final time of $t_{\max} = 1$ employing a timestep of $\Delta t = 0.2 \times \text{CFL} \times \Delta x_{\min}/c$ (a timestep fine enough so that the errors are dominated by their respective spatial discretization sizes). [Figure 6](#) presents the L^∞ errors (maximum errors over all space and time) for both the new FC solver as well as fourth- and sixth-order finite differences (all three employing the same time integration method). Such errors are calculated (e.g. for η) by the expression given by

$$L^\infty \text{ error} = \frac{\max_{x,t} (|\eta(x, t) - \eta_{\text{ref}}(x, t)|)}{\max_{x,t} (|\eta_{\text{ref}}(x, t)|)}. \quad (29)$$

As expected by construction (using $R = L = 5$ matching points for the Gram polynomial basis), the tests here indicate that the FC method converges at a fifth-order rate to 10^{-8} . After this point, the rate of convergence is observed to slow down as errors begin to be dominated by the timestep choice at a maximum CFL constant. This limit can be pushed to 10^{-10} or below by further refining the timestep well below the CFL condition such that errors are fully dominated by the spatial discretization (as have been observed for other FC-based methods [\[28\]](#)). Future work entails improving the current limit, possibly by investigating the construction of the interpolating polynomial basis as well as investigating the choice of spectral filter [\[21\]](#). Although sixth-order FD converges at an (expectedly) higher rate, the following section demonstrates that it still incurs numerical pollution errors that accumulate and make it less performant for long-time or long-distance propagation.

Convergence in 2D can be similarly assessed: consider a 2D manufactured solution given by

$$\begin{cases} \eta(x, y, t) = \sin(7x + 3y - 2t) \sin(2x + 11y - 1.2t), \\ u(x, y, t) = \cos(1.5x + 5.5y - t) \cos(9x + 0.5y - 1.1t), \\ v(x, y, t) = \sin(5x + 2.3y - 3t) \cos(3x + 7.5y - 1.3t). \end{cases} \quad (30)$$

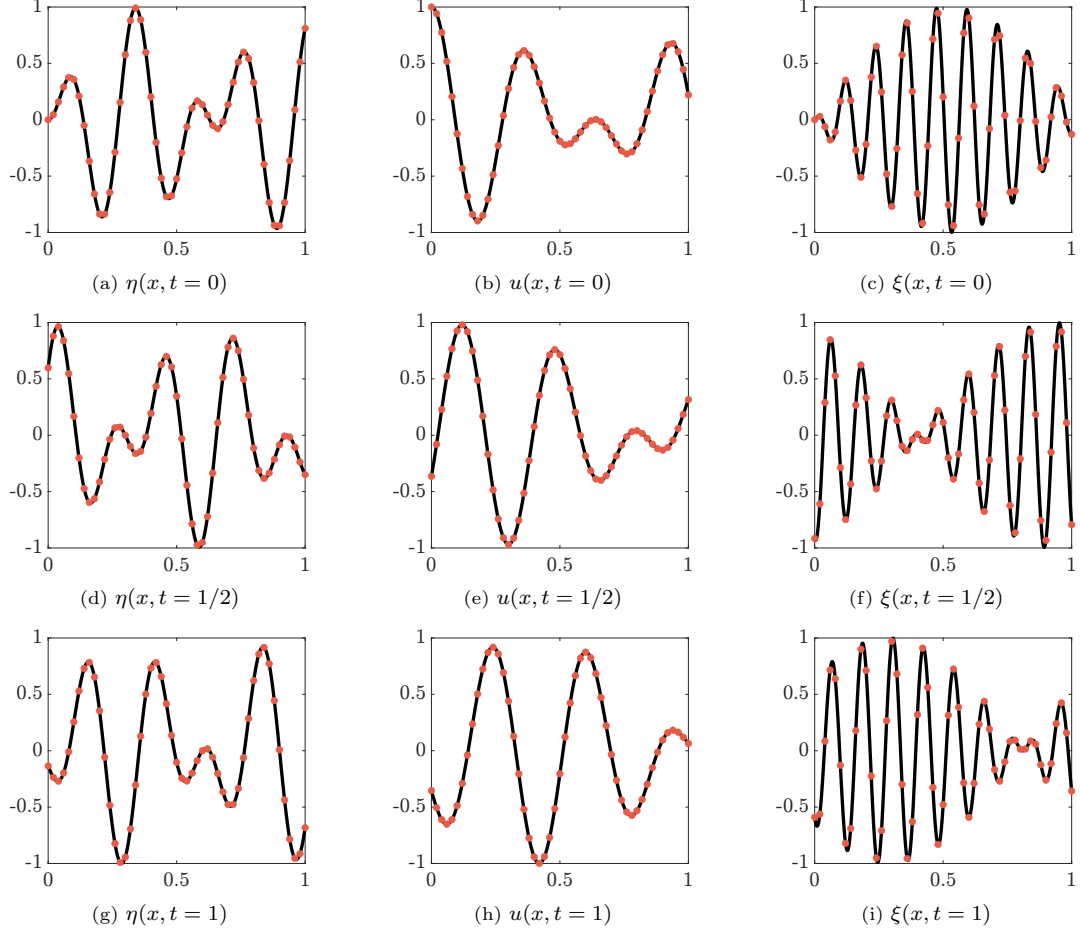


Figure 5: *Convergence studies*. Snapshots at various times of the manufactured solution corresponding to Eq. (27) and Eq. (28). Red dots denote the discretization corresponding to the coarsest mesh size employed in the convergence analysis.

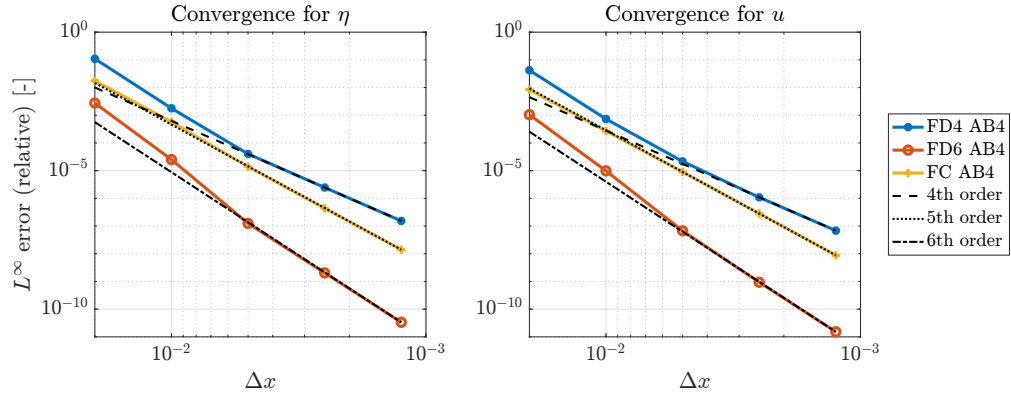


Figure 6: *Convergence studies*. Errors as a function of increasing spatial resolution for FC, FD4, and FD6 applied to the 1D problem corresponding to the exact solution given by Eq. (27) and Eq. (28).

Similarly to the 1D case, a highly dynamic ground motion, given by

$$\xi(x, y, t) = \sin(3x + 19y - 13t) \sin(27x + 5y - 15t), \quad (31)$$

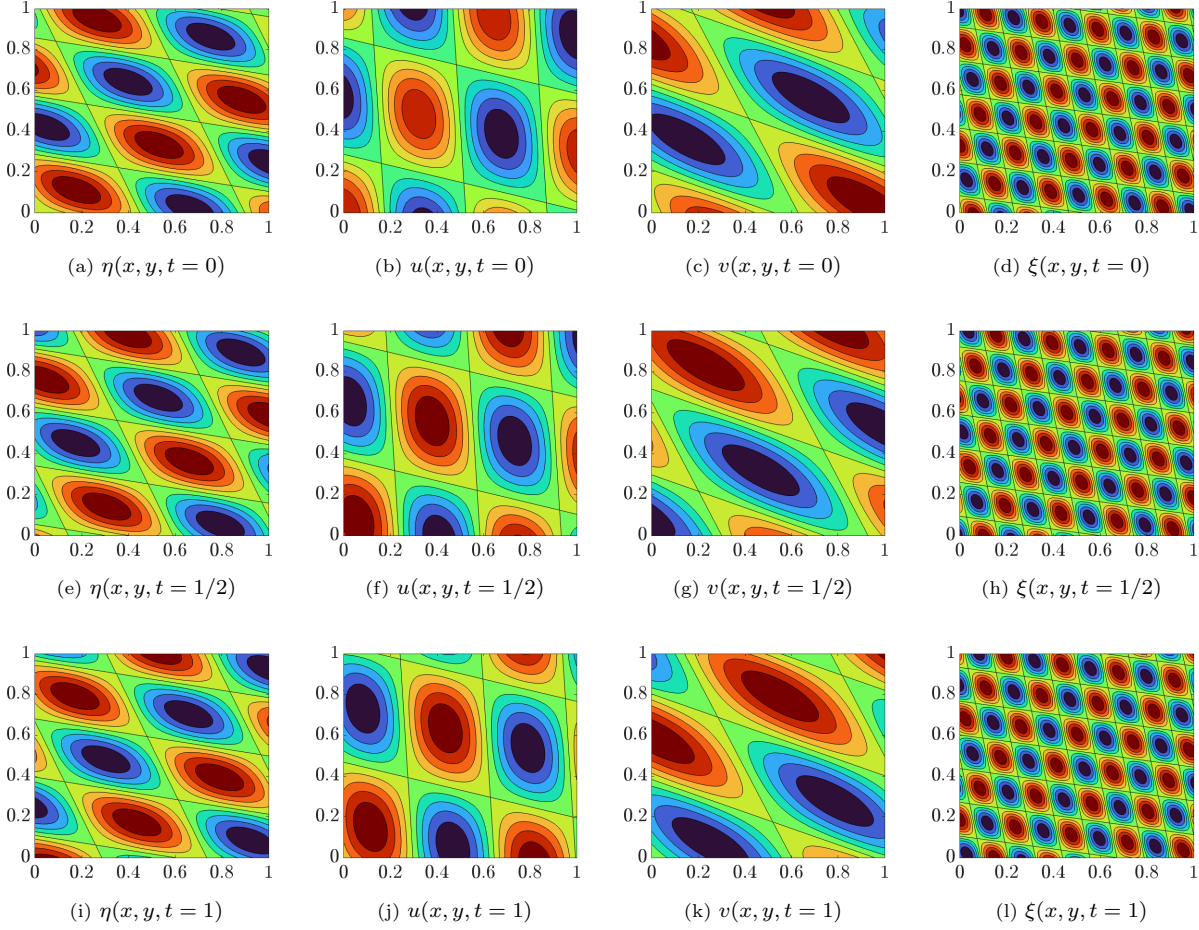


Figure 7: *Convergence studies.* Snapshots at various times of the 2D manufactured solutions corresponding to Eq. (30) and Eq. (31). The color scale ranges from -1 (dark blue) to 1 (dark red).

is imposed on the sea floor (chosen, again, to be faster and of higher frequency than the solutions of Eq. (30) in order to mimic realistic seismic scenarios). Snapshots in time of the manufactured solutions η , u and ξ are presented in Figure 7. Simulations are again performed employing $g = 1$ for a sequence of finer discretizations in both x and y , i.e., $\Delta x = \Delta y = 0.025, 0.0125, 0.00625, 0.003125$. Similarly to the 1D case, the final time is taken to be a complete cycle, i.e., $t_{\max} = 1$, employing a timestep that is one-fifth of the maximum allowable timestep from the CFL condition (Section 3.4) so that errors are dominated by the spatial discretization. Figure 8 presents the L^∞ errors (maximum errors over all space and time) for both the 2D FC solver as well as fourth- and sixth-order finite differences (all three employing the same time integration method). As expected by construction (using $R = L = 5$ matching points for the Gram polynomial basis), the FC method converges at the expected fifth-order rate, verifying the 2D solver implementation.

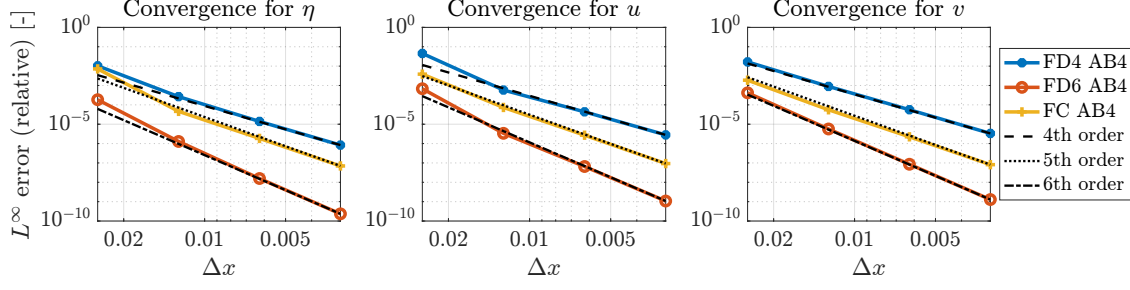


Figure 8: *Convergence studies.* Maximum errors over all space and time in η (left), u (middle), and v (right), as a function of increasing spatial resolution, for FD4 (blue), FD6 (orange), and FC (yellow) applied to the 2D problem whose exact solution is given by Eq. (30) and Eq. (31). Here, $\Delta y = \Delta x$.

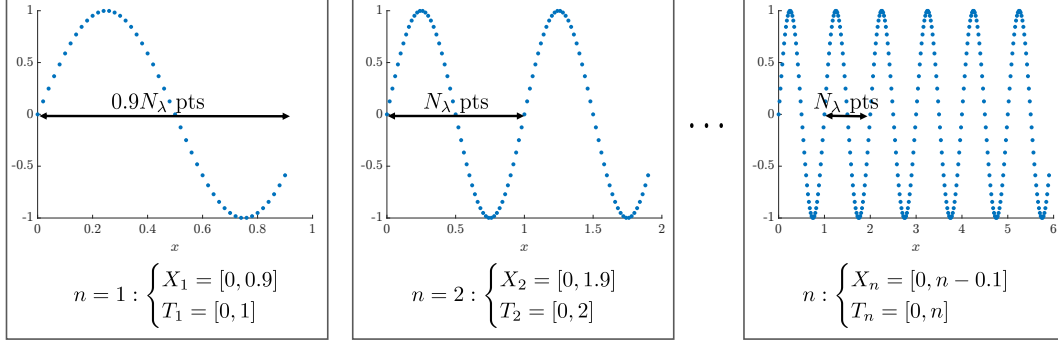


Figure 9: *Dispersion studies.* Illustrations of the manufactured free surface displacement given by Eq. (32) employed for assessing numerical dispersion, as a function of increasing problem size n , for a fixed discretization of N_λ points per wavelength.

4.2. Dispersion experiments

Numerical dispersion (or "pollution") errors of the FC-based solver can be studied and compared with other methods by considering a manufactured solution in the form of a propagating sine wave given by

$$\begin{cases} \eta(x, t) = \sin(2\pi(x - t)), \\ u(x, t) = \cos(2\pi(x - t)), \end{cases} \quad (32)$$

on the space-time intervals corresponding to $x \in X_n = [0, n - 0.1]$ and $t \in T_n = [0, n]$ for a number $n \in \mathbb{N}^*$ of wavelengths in the spatial domain, where each wavelength is discretized with a number N_λ of points per wavelength. The temporal interval is chosen to correspond to a full temporal cycle of the solution given by Eq. (32), and the spatial domain is defined on the slightly smaller interval $([0, n - 0.1])$ than the interval of periodicity $([0, n])$ in order to ensure the relevance of employing the FC procedure. The still water depth is taken to be $h_0(x) = 5$ throughout the domain, and no ground motion is considered (i.e., $\xi(x, t) = 0$ at all times). Snapshots of the solutions corresponding to increasing values of n at a fixed discretization of N_λ points per wavelength are presented in Figure 9.

As n increases, the solution propagates over a longer distance (and a correspondingly longer time interval). For the following tests, two fixed numbers of points per wavelength (i.e., resolution) are considered: $N_\lambda \in \{20, 50\}$ (corresponding to a spatial discretization of $\Delta x = 1/N_\lambda$). The timestep is chosen accordingly for each problem size via the CFL condition (see Section 3.4). Figure 10 presents the maximum L^∞ errors as a function of increasing problem size (i.e., n , for up to $n = 40$ wavelengths), comparing both FC and FD.

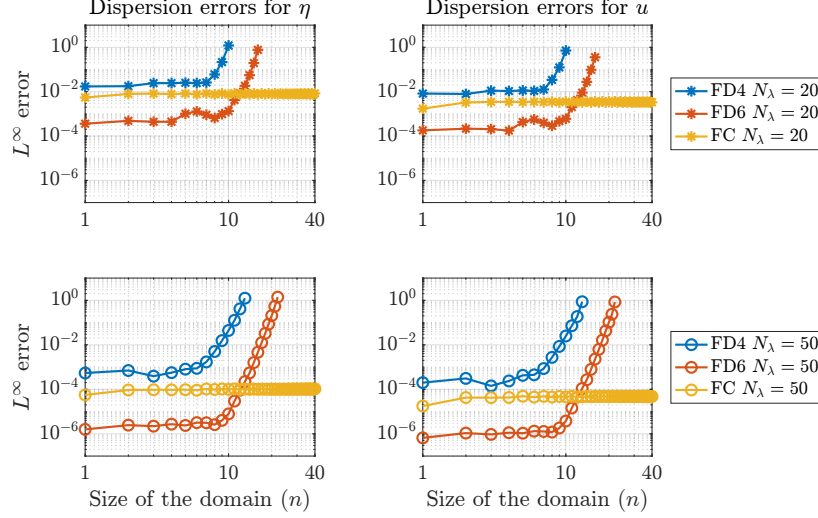


Figure 10: *Dispersion studies*. Maximum errors over all space and time in η (left) and u (right), as a function of increasing problem size n , for FD4 (blue), FD6 (orange), and FC (yellow) applied to the problem whose exact solution is given by Eq. (32). Two different numbers of fixed points per wavelength, N_λ , are considered: $N_\lambda = 20$ (top row) and $N_\lambda = 50$ (bottom row).

Such errors are calculated over all space and all time by the L^∞ norm given by Eq. (29).

Clearly, the error of FD increases with increasing n , eventually leading to instability when errors reach levels where the corresponding solutions violate the constraint $h > 0$ of the shallow water system. Such errors begin to grow after a certain size, even when increasing the FD stencil from fourth to sixth order (a higher order than FC and much higher than those commonly-used in FD-based tsunami solvers) or by increasing the number N_λ of points per wavelength. Indeed, FD and FEM-based methods are well-known to incur numerical dispersion/pollution errors [17, 18], requiring a substantial refinement of the corresponding meshes in order to capture solutions within a given accuracy for long-time and long-distance propagation. On the other hand, the error from the proposed FC-based solver remains constant, implying that it successfully avoids these pollution errors. This results in a level of error that is solely determined by the number of points per wavelength, no matter the problem size, which is very appealing for treating large-scale wave propagation problems.

Table 1 presents values of the errors and computational times for FC-based simulations corresponding to different combinations of problem sizes n and characteristic discretizations N_λ (i.e., three of the points found in the FC error curves of Figure 10). Additionally presented are the corresponding discretizations and computational times that are required for FD4-based and FD6-based simulations to achieve similar errors as FC. For $n = 20$ wavelengths at a discretization of $N_\lambda = 20$ points per wavelength ("Test 1"), FC achieves its errors with far fewer points (4.5 times fewer than FD6 and 31.5 times fewer than FD4) and significantly shorter runtimes (around 211 times faster than FD4 and around 6.5 times faster than FD6). Even when increasing the number of points per wavelength N_λ , a similar speedup is observed ("Test 2"). The qualities of FC with respect to numerical dispersion errors are further evident when increasing the problem size to a higher frequency, from $n = 20$ wavelengths to $n = 30$ wavelengths ("Test 3"): its speedup factor increases from 9 to almost 165 even when compared to an ostensibly higher-order method such as FD6 (which, for this test, still incurs five times larger errors than FC at the given discretization).

Test	Method	n	N_λ	CFL	η error [%]	u error [%]	T_{solve} [s]
1	FC	20	20	0.17	7.74×10^{-1}	3.45×10^{-1}	2
	FD4	20	650	0.21	7.76×10^{-1}	5.75×10^{-1}	422
	FD6	20	89	0.18	8.71×10^{-1}	4.35×10^{-1}	13
2	FC	20	50	0.17	1.10×10^{-2}	4.70×10^{-3}	3
	FD6	20	189	0.18	1.10×10^{-2}	5.00×10^{-3}	27
3	FC	30	20	0.17	8.03×10^{-1}	3.47×10^{-1}	3
	FD6	30	520	0.18	7.15×10^{-1}	3.56×10^{-1}	494

Table 1: *Dispersion studies.* Numerical discretization sizes (in terms of the number of points per wavelengths, N_λ) and computational times (in seconds) required by FD4 or FD6 to achieve similar errors as the FC-based solver (relative to the exact solution in Eq. (32)) for problem sizes of various numbers of n wavelengths.

5. Benchmarks

In what follows, the numerical implementation of the FC-based methodology is further validated, and its physical accuracy established, through applications of the solver to a number of (classical and non-classical) benchmark problems for a wide range of realistic configurations previously proposed by others.

5.1. Benchmark 1: Perturbation of a lake at rest

A classical validation of SWE solvers is to verify that the model satisfies a “lake at rest” configuration [49–51]. Such a benchmark consists of defining a sea floor topography with a still water height and verifying that the free surface remains exactly zero. In the context of the present solver, the shallow water system does not generate perturbations coming from a topography associated with a flat (zero initial water height) free surface. Hence, in a similar spirit, the lake at rest benchmark can be modified and adapted for other methods by employing, instead, an initial perturbation of the free surface, as proposed by LeVeque [52] and illustrated in Figure 11. An initial water height perturbation $\epsilon > 0$ is imposed on a portion of the free surface, i.e.,

$$\eta(x) = \begin{cases} \epsilon, & x_1 \leq x \leq x_2 \\ 0, & \text{otherwise,} \end{cases} \quad (33)$$

with a corresponding seafloor topography $s(x)$ given by

$$s(x) = \begin{cases} s_0 (\cos(\pi(x - x_3)/\alpha) + 1), & |x - x_3| < 0.1 \\ 0, & \text{otherwise.} \end{cases} \quad (34)$$

The problem formulation is non-dimensionalized, where the still water height is given by $h_0(x) = D - s(x)$ for a constant $D \in \mathbb{R}$.

Figure 12 presents snapshots at various times of the free-surface displacement produced by the FC-based solver, an FD4 a FD4 solver, and an FD6 solver for perturbations of size $\epsilon = 0.01$ (left) and $\epsilon = 0.2$ (right) and benchmark parameters corresponding to $D = 1$, $g = 1$, $s_0 = 0.25$, $x_1 = 0.1$, $x_2 = 0.2$, $x_3 = 0.5$, and $\alpha = 0.1$. All simulations are conducted on a spatial interval $x \in [-1, 1]$ employing $\Delta x = 0.01$ and $\Delta x = 0.00125$. The boundary conditions are set as walls (see Eq. (4)). The timesteps correspond to the maximum allowable by the respective CFL conditions (see Section 3.4) of each method employed. Overlaid in black for each figure is the reference free surface obtained by the quasi-steady wave-propagation method extracted from LeVeque’s results [52]. Here, both FD4 and FD6 suffer from spurious oscillations throughout the domain due to the initial condition and subsequently discontinuous solution. Even after refining the

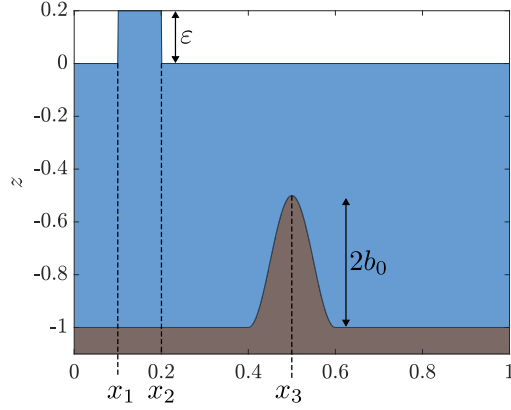


Figure 11: *Benchmark 1*. The perturbed lake-at-rest configuration proposed by LeVeque [52]. The total water depth is represented in blue, and the ground topography is represented in brown.

solution (eight times), such oscillations persist. However, even without any special treatment of such jumps, the FC-based solver, for the same discretizations as FD4 and FD6, still correctly captures the overall shape and form of the traveling perturbation after its interaction with the topographic bump (the non-flat region of the bathymetry), with no discernible oscillations away from it (treatment of discontinuities/shocks is a subject of future work and beyond the scope of the present solver). Indeed, overall results agree well with those presented in the original work [52], and only minor oscillations, that are confined very locally near the regions of sharpest curvature and are due to the truncation of the discrete Fourier series, are observable.

5.2. Benchmark 2: 1D tsunami

A second classical benchmark problem [38, 53] concerns the shallow water propagation of a tsunami towards a sloping beach in order to mimic a more realistic tsunami configuration. An illustration of the problem setup is presented in Figure 13. Over a domain $x \in [0, x_{max}]$, the initial condition is a solitary wave centered at $x = x_2$ and is given by

$$\eta(x, 0) = A \operatorname{sech} \left(\sqrt{\frac{3}{4D^2}} (x - x_2) \right) \quad (35)$$

for a constant $D > 0$ and wave amplitude (from the free surface) $A > 0$. The fluid is considered to be initially at rest, i.e. $u(x, 0) = 0$, and the corresponding bathymetry is given by

$$h_0(x) = \begin{cases} D + \frac{B}{x_1} (x - x_1), & 0 \leq x \leq x_1 \\ D, & x \geq x_1, \end{cases} \quad (36)$$

where $x_1 \in \mathbb{R}$ demarcates the beginning of the sloping beach. Since such a bathymetric formulation is only piecewise continuous, the results that follow employ a standard C^∞ rounding of Eq. (36) through the use of hyperbolic tangents. The corresponding boundary conditions are considered to be radiation boundary conditions (see Eq. (5) at both the left and right boundaries.

Figure 14 presents solution snapshots at various times produced by the FC solver for values of $A = 30$ m, $D = 5.04$ km, $B = 5.00$ km, $x_1 = 20$ km, and $x_2 = 50$ km (all parameters adopted from [38]). The gravitational constant is taken to be $g = 9.81$ m/s². The simulation is conducted on a spatial interval

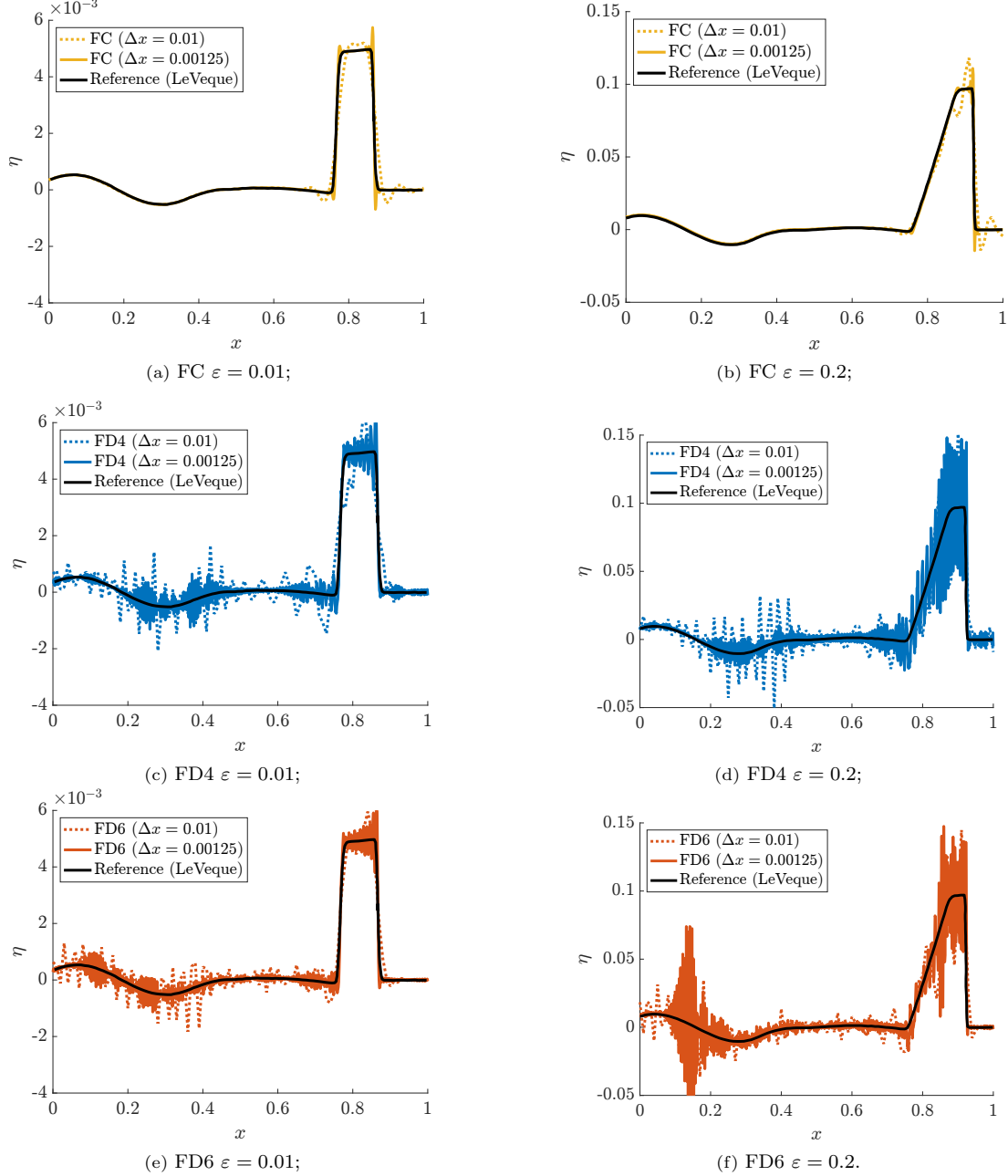


Figure 12: *Benchmark 1*. Free surface displacement snapshots at $t = 0.7$ for FC (top), FD4 (middle), and FD6 (bottom) at various discretizations. Reference solutions are given by the second-order finite volume solver of [52].

$x \in [0.2, 100.0]$ km employing a discretization size of $\Delta x = 671$ m ($N_x = 150$ points, similarly to [38]). The corresponding timestep is taken to be $\Delta t = 0.511$ s, and the solution is evolved up to a final time of $t = 500$ s. The initial condition of Figure 14a splits into two waves propagating towards each end of the domain (Figure 14b). The left-going wave propagates until it encounters the sloping beach, reaching maximal amplitude at the left boundary as illustrated in Figure 14c, while the right-going wave passes out of the region of interest (here, after 100 km [38]). Figure 14d illustrates the reflected wave from the left

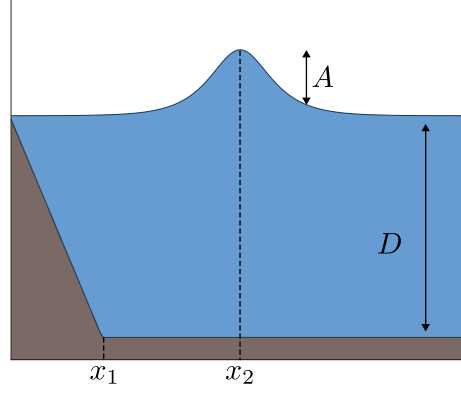


Figure 13: *Benchmark 2*. The 1D tsunami configuration proposed by Setiyowati and Sumardi [38]. The total water depth is represented in blue, and the ground topography is represented in brown. The free surface displacement is amplified for visualization ($\times 50$).

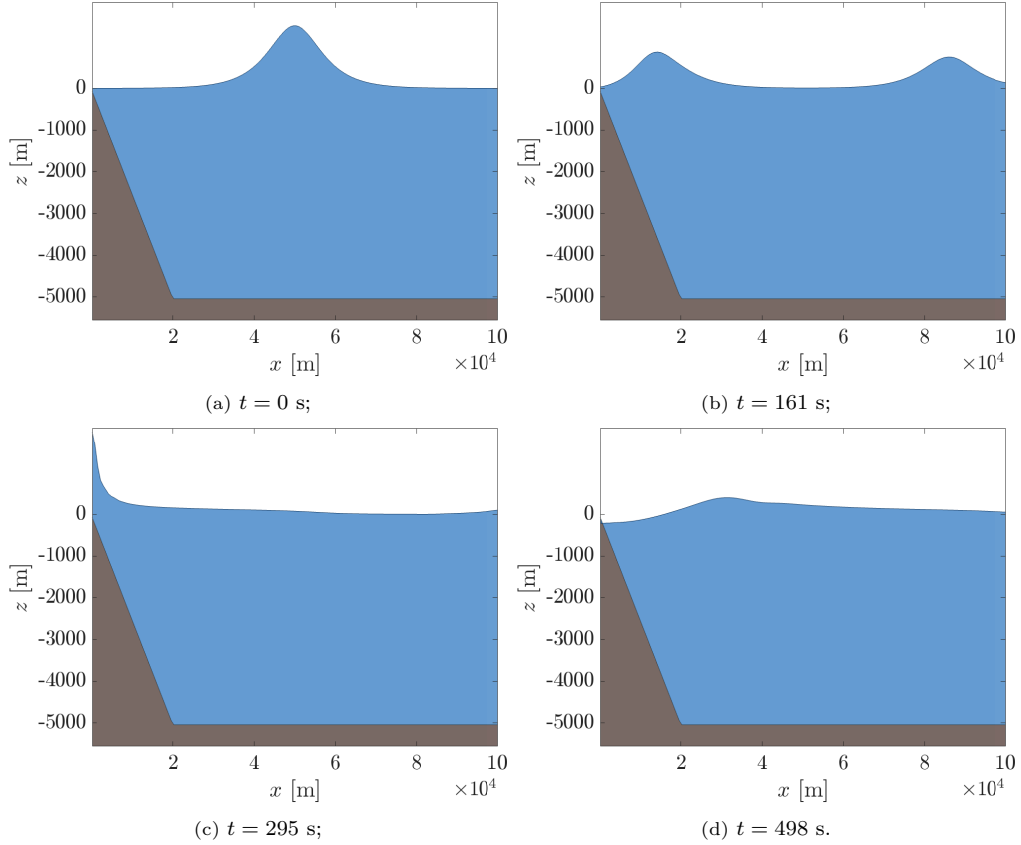


Figure 14: *Benchmark 2*. Snapshots at various times of the water perturbation η around the mean free surface $z = 0$ produced by the FC solver. The total water depth is represented in blue, and the ground topography is represented in brown. The free surface displacement is amplified for visualization ($\times 50$).

boundary propagating back towards the right into the water.

Figure 15 presents the complete space-time evolution of the left-going and right-going traveling waves in terms of a pseudocolor plot. The FC-based simulation agrees well with the reference study [38] in terms of propagation times and wave heights. Overlaid on the figure is the theoretical approximation of the speeds

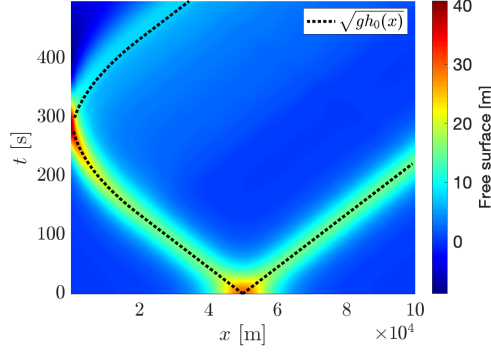


Figure 15: *Benchmark 2*. The complete space-time evolution of the tsunami waves (left-going towards the sloping beach) produced by the FC-based solver. Overlaid in black is the expected approximate wave speed, $c = \sqrt{gh_0(x)}$, given by linear theory [36].

of the left-going and right-going waves (given by linear wave theory [36] as $c = \sqrt{gh_0}$ for still water depth h_0). Here, the FC-based solution tracks well with the expected linear theory, including with the expected slow down of the left-going wave as it approaches and climbs the sloping beach.

A more quantitative assessment relates to mass conservation. The area (or "volume") displaced at a time t is given by

$$V_{1D}(t) = \int_{x_{\min}}^{x_{\max}} \eta(x, t) dx. \quad (37)$$

The corresponding percentage error from an initial time $t_{\min} = 0$ to a final time t_{\max} (when the left-going wave is entirely reflected) is hence given by

$$\varepsilon_{mc} = \left(\frac{V_{1D}(t_{\max})}{V_{1D}(t_{\min})} - 1 \right) \times 100. \quad (38)$$

The FC-based solution using the same $\Delta x = 671$ m discretization (corresponding to $N_x = 150$ points per 100 km) yields a mass conservation error $\varepsilon_{mc} = 0.058\%$. For reference, increasing the discretization to $N_x = 5000$ points per 100 km reduces this error to a value of $\varepsilon_{mc} = 0.0000025\%$, implying high-order convergence. In both cases (coarse and fine), mass conservation is effectively preserved numerically and converges. Indeed, such values fall significantly below the mass conservation tolerances as set forth in the standards of the National Oceanic and Atmospheric Administration (NOAA) [54], which defines appropriate numerical conservation as when the final volume is within 5% of the initial displaced volume.

5.3. Benchmark 3: 2D steady vortex

A third benchmark [50] concerns a 2D FC-based evaluation of the shallow water equations applied to a problem of a steady vortex and its comparison to a high-order finite volume (FV) treatment from [50]. Over a spatial domain $(x, y) \in [-3, 3] \times [-3, 3]$ and employing a gravitational constant $g = 9.81$ m/s², the initial free surface and velocity field are given by

$$\begin{cases} \eta_0(x, y) = -\frac{1}{4g} \exp(2(1 - (x^2 + y^2))), \\ u_0(x, y) = y \exp(1 - (x^2 + y^2)), \\ v_0(x, y) = -x \exp(1 - (x^2 + y^2)), \end{cases}, \quad (39)$$

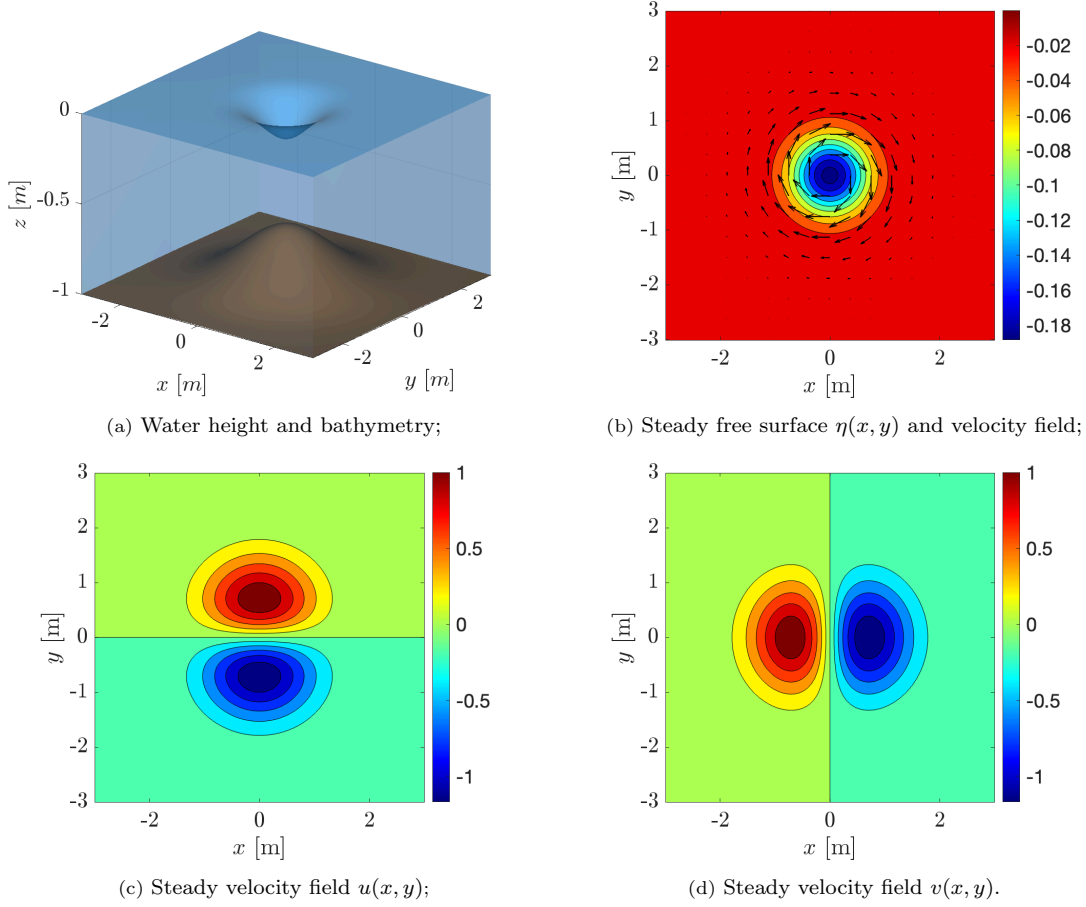


Figure 16: *Benchmark 3*. Illustration of the overall configuration from [50] corresponding to the analytical solution given by Eq. (39).

where boundary conditions are chosen to be the same. The considered bathymetry is a Gaussian bump given by

$$h_0(x, y) = -0.2 \exp(0.5(1 - (x^2 + y^2))). \quad (40)$$

The solution to such a problem is the (exact) steady solution given by

$$\begin{cases} \eta(x, y, t) = \eta_0(x, y), \\ u(x, y, t) = u_0(x, y), \\ v(x, y, t) = v_0(x, y). \end{cases} \quad (41)$$

Figure 16 presents the overall problem setup alongside solution snapshots for the free-surface displacement $\eta(x, y)$ (Figure 16b) and velocity field $(u(x, y), v(x, y))^T$ (Figures 16c-16d) given by Eq. (41).

Table 2 presents the absolute L^∞ errors (over all space and time up to $t_{\max} = 1$ s) for the free surface $\eta(x, y, t)$ of simulations produced by the FC-based solver applied to increasing spatial discretizations of size $N = N_x N_y$. For reference, the corresponding errors from [50] employing FV are additionally reported using the very same discretizations. The high-order convergence of FC can be observed (up to seventh order), leading to errors that are orders-of-magnitude lower than the reference FV values from [50] (at the same fine

N	FC L^∞ error	FC order	FV L^∞ error (from [50])	FV order (from [50])
1 024	1.13×10^{-3}	-	5.52×10^{-2}	-
4 096	9.87×10^{-6}	6.99	1.68×10^{-2}	1.72
16 384	7.75×10^{-8}	7.07	5.00×10^{-3}	1.75
65 536	6.01×10^{-10}	7.05	1.40×10^{-3}	1.84
262 144	1.02×10^{-11}	5.90	3.77×10^{-4}	1.89

Table 2: *Benchmark 3*. Maximum errors and convergence rates of the free surface displacement $\eta(x, y, t)$ for the steady vortex problem treated by the FC-based solver and reference values corresponding to the highest order of finite volume (FV) employed in [50].

N	FC L^∞ u -error	FC L^∞ v -error	Time [s]
1 024	5.06×10^{-3}	5.09×10^{-3}	0.2
4 096	4.58×10^{-5}	4.60×10^{-5}	0.5
16 384	3.74×10^{-7}	3.75×10^{-7}	2.1
65 536	1.26×10^{-8}	1.26×10^{-8}	14.0
262 144	2.07×10^{-9}	2.07×10^{-9}	102.1

Table 3: *Benchmark 3*. Maximum errors and computing times (MATLAB, see Section 3.4), as a function of increasing spatial discretization, for the two velocity components $u(x, y, t)$ and $v(x, y, t)$ produced by the FC-based solver.

discretization of $N = 262\,144$, around 37 million times more accurate). Similarly low errors can be observed in Table 3 for the velocity fields simulated by the FC solver (errors for such components are not provided in [50]), which additionally presents the corresponding computation times in MATLAB (not provided for the reference FV solutions in [50]).

5.4. Benchmark 4: 2D tsunami propagation

A fourth benchmark problem [55] concerns the 2D propagation of an N-wave, which is a typical (realistic) shape of observed tsunami waves. Such a benchmark is used as a reference at the International Atomic Energy Agency [56] (IAEA) for evaluating the performance of academic tsunami solvers [15, 57]. Over a domain $(x, y) \in [-100, 100] \times [-100, 100]$ (meters), the initial condition has the form of an N-wave given by

$$\eta_0(x, y) = \frac{\varepsilon H}{2} [\tanh(\gamma(x - x_0)) - \tanh(\gamma(x - x_0 - L))] (y - y_2) \operatorname{sech}^2(\gamma(y - y_1)) \quad (42)$$

for positions $x_0, y_1, y_2 \in \mathbb{R}$ and coefficients $\varepsilon, \gamma, H, L \in \mathbb{R}^+$. The problem admits an exact analytical solution to the *linearized* shallow water equations [55] that is given by

$$\eta(x, y, t) = \frac{1}{(2\pi)^2} \int_{-\infty}^{\infty} \int_{-\infty}^{\infty} \hat{\eta}_0(k, l) e^{i(kx + ly)} \cos(\omega t) \, dk \, dl \quad (43)$$

for $\omega = \sqrt{k^2 + l^2}$. Here, $\hat{\eta}_0$ is the Fourier transform of the initial condition and is given by [55]

$$\hat{\eta}_0(k, l) = i \frac{4\varepsilon H}{\pi} \alpha^3 (e^{-ikL} - 1) e^{-i(kx_0 + ly_1)} [(y_1 - y_2)l + i(1 - \alpha l \coth(\alpha l))] \operatorname{cosech}(\alpha k) \operatorname{cosech}(\alpha l) \quad (44)$$

for $\alpha = \pi/(2\gamma)$.

Figure 17 presents the initial and final temporal snapshots in 2D of the solutions obtained by the FC-solver for a simulation conducted on a discretization of size $N_x = N_y = 201$ and advanced up to a time $t = 60$ s. The boundary condition are set as radiation (see Eq. (9)). All parameters of the initial condition are adopted from [15, 56, 57] and correspond to $h_0 = 1$ m, $g = 1$ m/s², $H = 0.001$ m, $L = 30$ m, $y_1 = 0$ m, $y_2 = 2.3$ m, $x_0 = -15$ m, $\epsilon = 0.004$, and $\gamma = 0.1061$ (unitless).

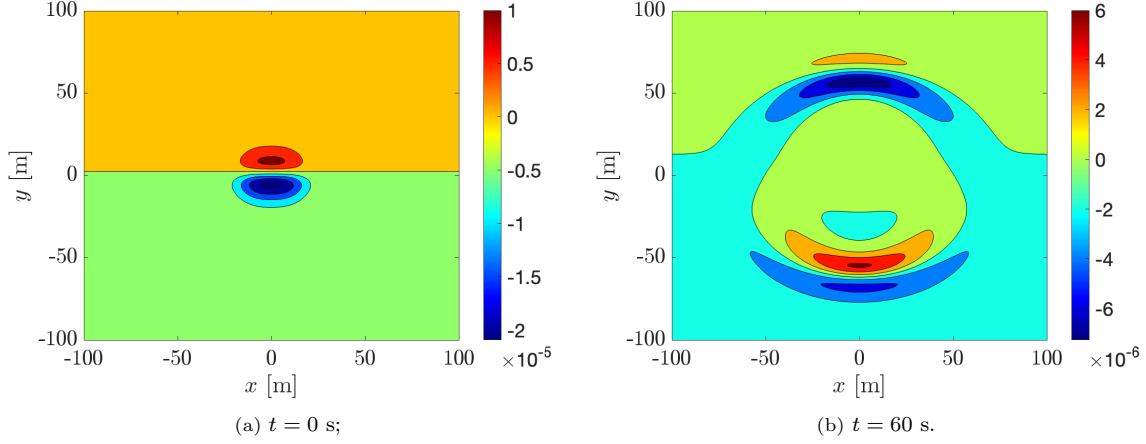


Figure 17: *Benchmark 4*. Snapshots of initial condition ($t = 0$ s) and last timestep ($t = 60$ s) produced by the FC-based solver for the N-wave configuration.

Figure 18 additionally presents temporal snapshots slice-wise at $x = 0$ m for times $t = 0, 20$ and 60 s (corresponding to the same as those considered in [15, 57]). The analytical (linearized) solution given by Eq. (43) is overlaid in red, demonstrating excellent qualitative agreement with the solutions produced by the FC solver in black. The corresponding maximum L^∞ errors over all time and space, given by (in percentage)

$$\varepsilon_{\%}(t) = \frac{\max_{x,y} (|\eta(x,y,t) - \eta_{\text{ref}}(x,y,t)|)}{\max_{x,y,t'} (|\eta_{\text{ref}}(x,y,t')|)} \times 100, \quad (45)$$

are found to be $\varepsilon_{\%} = 5.62 \times 10^{-3} \%$ and $\varepsilon_{\%} = 2.82 \times 10^{-2} \%$ up to time $t = 20$ s and $t = 60$ s, respectively. It should be noted that these errors are computed with respect to an exact solution of the *linearized* shallow water equations [55], and hence cannot be reasonably expected to converge using the nonlinear shallow water equations that are treated in this work. In addition, the simplified non-reflecting boundary condition limits the order of convergence given by FC at the boundary. Nevertheless, the errors are below 0.03% over all space and all time.

5.5. Benchmark 5: waves generated by dynamic sea floor displacement

A final benchmark concerns the simulation of waves generated by fully dynamic motions of the seafloor (bathymetry movement) and their assessment versus experimental data. Such a configuration has been treated by other solvers [6, 58], and is inspired by the pioneering work of Hammack, et al. [59], which presented laboratory measurements of the water elevation caused by a moving source (a piston vertically displacing an interval of the seafloor). An illustration of the problem formulation is presented Figure 19 (the reader is referred to [59] for the corresponding experimental setup).

The unperturbed bathymetry $h(x) = h_0$ is considered initially flat and is then subjected to a dynamic perturbation that is given by

$$\xi(x,t) = f(t)\mathcal{H}(x^2 - x_1^2), \quad (46)$$

where $x_1 \in \mathbb{R}$ is the half-length of the piston and \mathcal{H} is the Heaviside function given by

$$\mathcal{H}(x) = \begin{cases} 1, & x \geq 0 \\ 0, & x < 0. \end{cases} \quad (47)$$

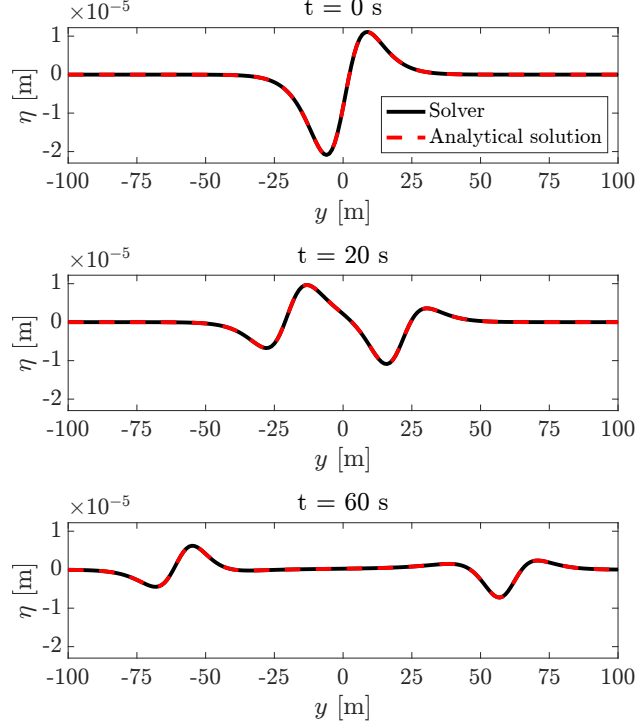


Figure 18: *Benchmark 4*. Snapshots at various times of the free surface displacement η produced by the FC-based solver (black) on the line corresponding to $x = 0$. Overlaid in red is the analytical solution from [55].

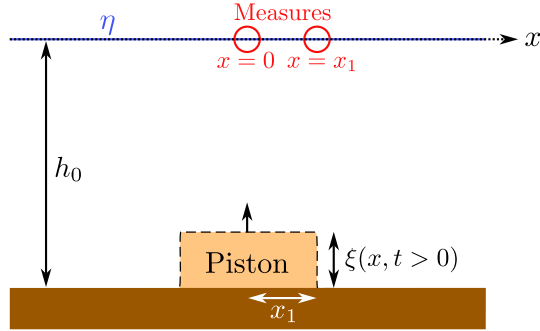


Figure 19: *Benchmark 5*. Illustration of the moving piston configuration inspired by [59].

The temporal function $f(t)$ is given by

$$f(t) = \begin{cases} 0, & t < 0 \\ \xi_m (1 - \cos(\pi t/t_r))/2, & 0 \leq t \leq t_r \\ \xi_m, & t > t_r, \end{cases} \quad (48)$$

for perturbation amplitude $\xi_m \in \mathbb{R}^+$ (i.e., the maximum piston height) and rising time $t_r \in \mathbb{R}^+$. The latter is given by a non-dimensionalized characteristic ratio $\tau = t_r/t_c \ll 1$ between the rise time t_r and the shallow water wave propagation time $t_c = x_1/\sqrt{gh_0}$ for characteristic length x_1 (the half-length of the piston). The initial conditions correspond to water at rest, i.e. $\eta(x, 0) = 0$, $u(x, 0) = 0$, and the boundary conditions are considered to be walls, i.e., $\eta_x = 0$ and $u = 0$ at the boundary (see Eq. (4)).

Remark 5.1. In order to retain the high-order nature of the FC-based solver introduced in this work, a smoothing of the rectangular perturbation (piston) is employed by approximating the Heaviside function \mathcal{H} by means of hyperbolic tangents, i.e.,

$$\mathcal{H}(x^2 - x_1^2) \approx \frac{1}{2} (\tanh(a(x + x_1)) - \tanh(a(x - x_1))),$$

with $a \ll 1$ (a value of $a = 0.01 \text{ m}^{-1}$ is employed in this section).

Employing $h_0 = 200 \text{ m}$, $g = 9.81 \text{ m/s}^2$, and non-dimensionalized values $x_1/h_0 = 12.2$ and $\xi_m/h = 0.4$, Figure 20 presents temporal snapshots of the solutions produced by FC (left column), FD4 (middle column), and FD6 (right column). All simulations are conducted over a (non-dimensionalized) domain $x/x_1 \in [-10, 10]$ up to a final (non-dimensionalized) time $t = t_{\max} \sqrt{g/h} = 69$, using the same discretization $N_x = 1001$ points and the maximum allowable timestep by each of the method's respective CFL conditions (Section 3.4). After being generated by the seafloor displacement caused by the moving piston, two waves propagate in each direction. Without any special treatment of the discontinuity or shock, the FC-based solution incurs very reasonable errors despite the sharp wave front. A slight error (that does not grow in time) can be observed at the water jump due to the lack of the highest-frequency Fourier modes in the discrete Fourier series. For finite differences, on the other hand, one can observe that the waves experience very large numerical oscillations at the sharp wave front (even though the stencils are of high order). Such high-frequency errors for FD4 and FD6 continue to grow in time as the waves propagate (Figure 20h and Figure 20i), illustrating that, in the case of such rapid sea floor motions, robust methods like FC may be better suited. Even with substantial refinements, such oscillations are not assured to be mitigated (see also the benchmark in Section 5.1).

Figure 21 presents the evolution of the free surface at the middle (left figure) and edge (right figure) of the piston, where available laboratory data are measured [59] and are presented alongside in red. Since dimensions of the physical experiments differ from the proposed simulated configurations [58] by orders of magnitudes (initial bathymetry depth here is $h_0 = 200 \text{ m}$, whereas in the laboratory depths ranged between 5 cm to 50 cm), all distances and times are presented in non-dimensionalized form. The results of the solver agree well globally with all observed measurements at both locations, with a maximum local error (L^∞ over time) of 32% and 20%, respectively. For reference, an approximate analytical solution is additionally presented in grey, derived from linear wave theory in the original work [59] and given by

$$\eta(x, t) = \frac{\xi_m}{\pi} \int_0^\infty \frac{\cos(kx) \sin(kb)}{k \cosh(kh)} \frac{\kappa^2}{\kappa^2 - \omega^2} [\cos(\omega t) - \cos(\kappa t) + \mathcal{H}(t - t_r) (\cos(\omega(t - t_r))) + \cos(\kappa t)] dk \quad (49)$$

for $\kappa = \pi/t_r$ and $\omega = \sqrt{gk \tanh(kh)}$. Such a solution evolves like a damped oscillatory system and is unable to adequately capture the (nonlinear) dynamic response. Indeed, this linear theory matches experimental results only for $\xi_m \ll h$ [58], which is not the case here given that $\xi_m/h = 0.4$.

6. A parametric case study on the effects of earthquake speeds on tsunamigenesis

The performance and physical accuracy of the proposed FC-based solver has been demonstrated through the rigorous numerical experiments of Section 4 and the benchmarks of Section 5. This section applies the solver on a realistic and understudied geophysical scenario in an effort towards further study of the dynamic effects of earthquakes (and their subsequent time-dependent velocities and displacements) on tsunamigenesis. Such a problem, introduced herein, is inspired by recent results that have suggested that some induced

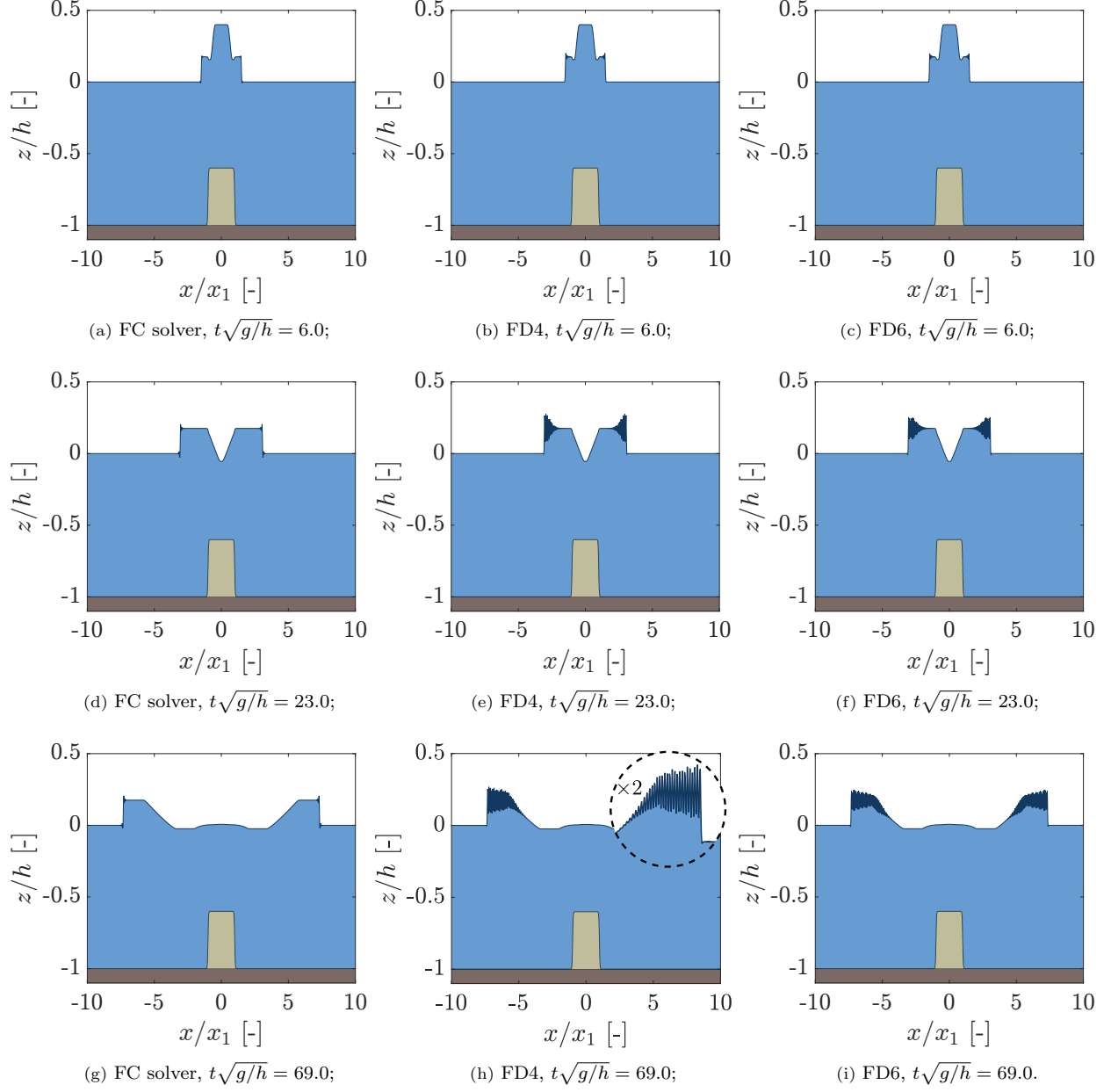


Figure 20: *Benchmark 5*. Snapshots at various times (each row) of the free surface displacement η produced by FC (left column), FD4 (middle column), and FD6 (right column). All simulations employ the same discretization of size $N_x = 1001$. The dynamic piston movement is already at maximum displacement at these times (yellow). No amplification scaling of the solution is presented here for visualization.

tsunami dynamics are linked to the corresponding time-dependencies of the earthquake sources [5, 6, 43]. The objective is to propose a novel problem configuration in order to investigate the influence of *earthquake speed* on tsunami generation, as well as to compare it to classical tsunami approaches that neglect time-dependent seafloor movements. To this end, two variations are presented as follows: a 1D formulation and a 2D formulation, both utilizing physically-realistic parameters inspired by an idealized subduction fault (perpendicular to the sea surface).

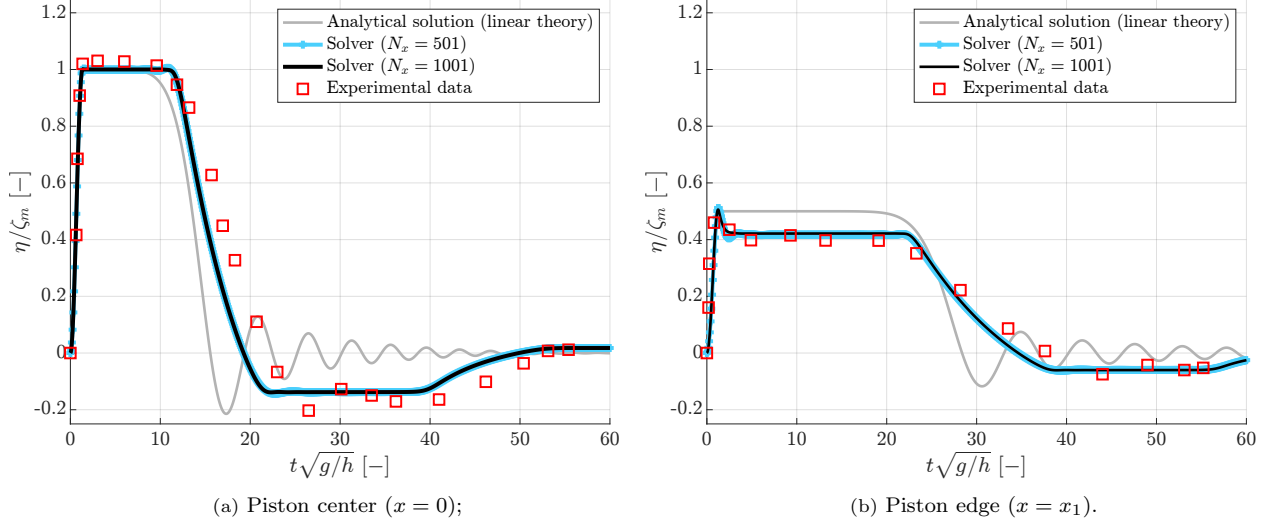


Figure 21: *Benchmark 5*. Time evolution of the normalized free surface displacement η at the center (left) and edge (right) of the piston, produced by the FC-based solver. Two discretizations are presented (in blue and black), demonstrating convergence of the solver and good correspondence to the experimental results (red squares) from [59]. The linearized analytical solution from [59] is additionally presented and demonstrates its limitations in comparison with the data.

6.1. 1D formulation

The fundamental novelty of the overall problem lies in the analysis of the effects of earthquake speeds on tsunamigenesis by considering sources mimicking ruptures, perpendicular to the sea floor, that propagate seismic waves and ultimately generate surface (Rayleigh) waves of parameterized speeds given by

$$c_{\text{eqk}} = n\sqrt{gH_0} \quad (50)$$

for integers $n \in \mathbb{N}^*$ (i.e., integer multiples of the characteristic tsunami propagation speed $\sqrt{gH_0}$). Such sources can be modeled as time-dependent sea floor displacements $\xi(x, t)$ in the shallow water equations that are given by

$$\xi(x, t) = \int_0^t \xi_t(x, \tau) d\tau, \quad (51)$$

where ξ_t is the time-derivative of the vertical displacement (i.e., vertical seafloor velocity) given by

$$\xi_t(x, t) = \frac{nA}{\sqrt{(x/L)^2 + \varepsilon^2}} \left[\exp\left(-\frac{(x - c_{\text{eqk}}t)^2}{2\sigma^2}\right) + \exp\left(-\frac{(x + c_{\text{eqk}}t)^2}{2\sigma^2}\right) \right] \quad (52)$$

for an amplitude scaling $A = 0.2$ m/s, a unitless regularization parameter $\varepsilon = 0.5$, pulse width $\sigma = 3$ km, a decay parameter $L = 20$ km to account for geometric attenuation of the surface waves. The general formulation described by Eq. (51) and Eq. (52) approximates these surface waves as the sum of two Gaussians propagating in opposite directions from a source centered at $x = 0$ m (the considered rupture location) and at speeds that are a given n integer multiples of the corresponding approximate tsunami speed ($\sqrt{gH_0}$). Such a problem configuration illustrates the two scales of tsunamigenesis considered in what follows: an earthquake surface wave propagating quickly with respect to the tsunami waves, but not quickly enough to neglect the earthquake dynamics. Figure 22 presents an example of the time evolution of this dynamic source for $c_{\text{eqk}} = 10\sqrt{gH_0}$ (i.e., $n = 10$ in Eq. (50)) given by Eq. (51) and Eq. (52), where numerical integration of the former is facilitated by a straightforward trapezoidal rule. For a depth of $H_0 = 4$ km (considered below),

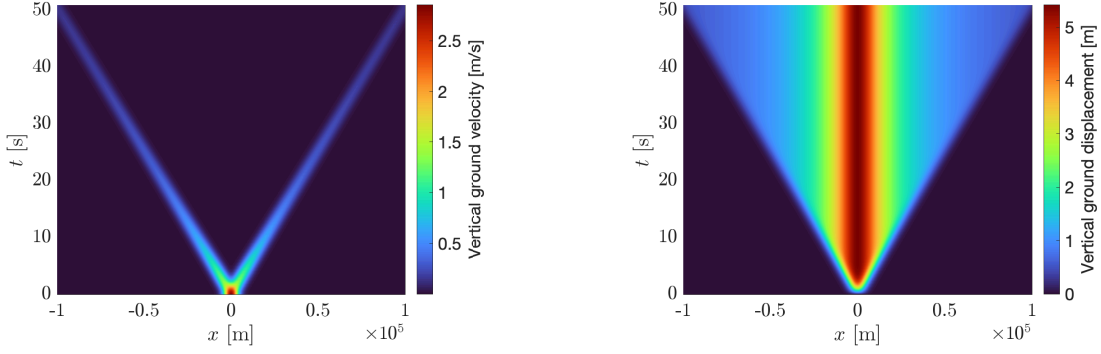


Figure 22: *1D earthquake-induced tsunamigenesis*. The dynamic source for an earthquake speed of $c_{\text{eqk}} = 10\sqrt{gH_0}$, in terms of velocity $\xi_t(x, t)$ (left) and displacement $\xi(x, t)$ (right), corresponding to the proposed problem configuration defined by Eq. (51) and Eq. (52).

such an example yields $c_{\text{eqk}} \approx 2$ km/s, approaching the Rayleigh wave speed.

Remark 6.1. *Seismogenic tsunamis are classically modeled by the final (static) vertical displacement (i.e., neglecting its time-dependence as well as its velocity), applied as an initial condition at $t = 0$ [4]. Although this approximation may be valid in the far-field (i.e., for long distance propagation), such sourcing may not be well-suited in the near-field (the primary motivation of this work and of the problem introduced here), possibly leading to considerable errors with implications on hazard assessment [4, 5]. For comparison, in all the results that follow for 1D and 2D, statically-sourced solutions are presented alongside the dynamically-sourced results at different earthquake speeds (both produced by the FC-based solver). This includes static displacements applied conventionally at $t = 0$ as well as instantaneous displacements at times $t = t_{\text{eqk}}$ (the latter following [5]), where t_{eqk} corresponding to the time at which the surface waves have achieved their final displacement in the domain for each earthquake speed c_{eqk} .*

Over a domain $x \in [-100, 100]$ km, the initial (unperturbed) bathymetry is that of a hyperbolic tangent beach, given by $h_0(x) = H_0 - s(x)$ for maximum depth $H_0 = 4$ km (close to typical mean ocean depth), where the initial seafloor topography $s(x)$ is given by

$$s(x) = \frac{S}{2} (1 - \tanh(a(x - x_1))) (x_1 - x) \quad (53)$$

for $x_1 = -85$ km, $a = 2 \times 10^{-4} \text{ m}^{-1}$ and $S = 3.99$ km. The initial condition corresponds to that of still water (i.e., $\eta(x, t = 0) = 0$, $u(x, t = 0) = 0$), and the boundary conditions are prescribed as non-reflecting (see Eq. (5)). Figure 23 presents snapshots at various times. produced by the FC-based solver, of the tsunami propagation and its ground motion source corresponding to an example earthquake speed of $c_{\text{eqk}} = 10\sqrt{gH_0}$, along with a visualization of the unperturbed bathymetry in Figure 23a. Such results are produced by a simulation that is advanced to a final time $t_{\text{max}} = 1000$ s at a spatial discretization corresponding to $N_x = 300$ points. Figure 24 presents the complete space-time evolution of the corresponding tsunami displacement $\eta(x, t)$ produced by the FC solver for such a source. One can observe two types of waves: the earthquake surface waves that propagate at $c_{\text{eqk}} = 10\sqrt{gH_0}$ and that reach the domain edge at around a time $t = 50$ s, and the tsunami waves with their longer wavelengths and slower speeds ($\sqrt{gH_0}$). The left-going tsunami wave slows down as $h_0(x) = H_0 - s(x)$ decreases with the approaching beach (similarly to the benchmark of Section 5.2).

In order to emphasize the importance of considering earthquake dynamics in tsunami modeling (the main motivation of the solver introduced in this work), Figure 25a presents the time evolution of water elevation

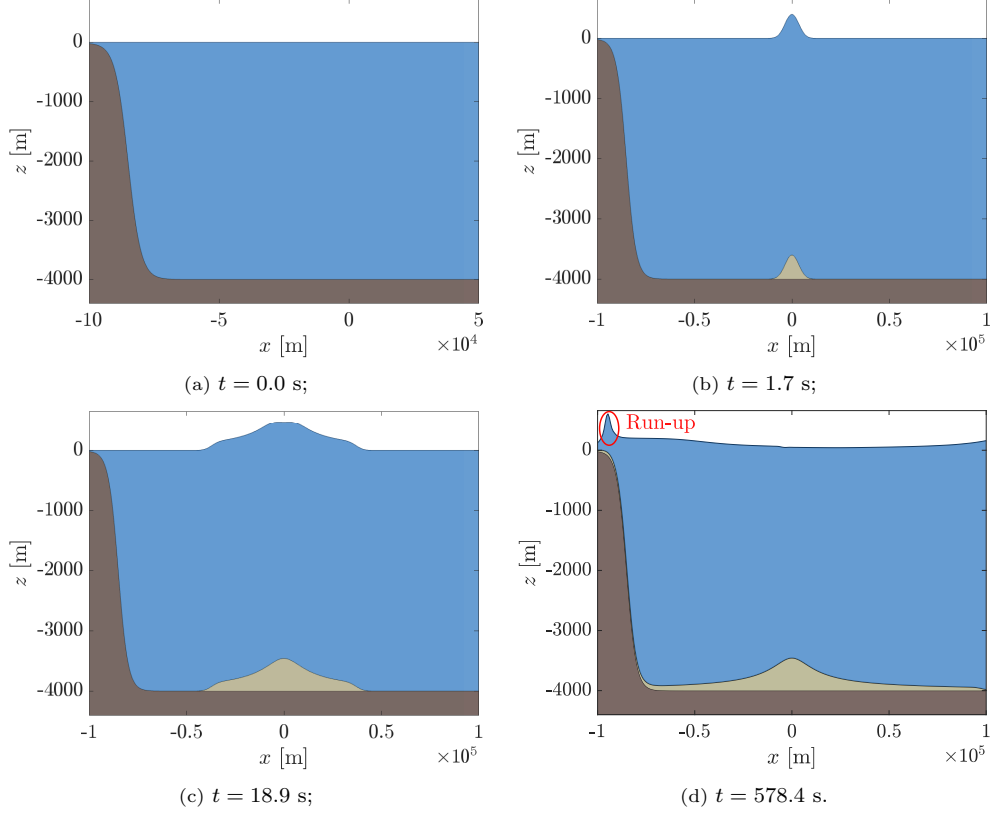


Figure 23: *1D earthquake-induced tsunamigenesis*. Snapshots at various times of tsunami generation and propagation (blue), including the dynamic earthquake source of speed $c_{\text{eqk}} = 10\sqrt{gH_0}$ (yellow). The last snapshot indicates the time/location at which run-up is evaluated. The free surface displacement and the ground perturbation are amplified for visualization ($\times 100$).

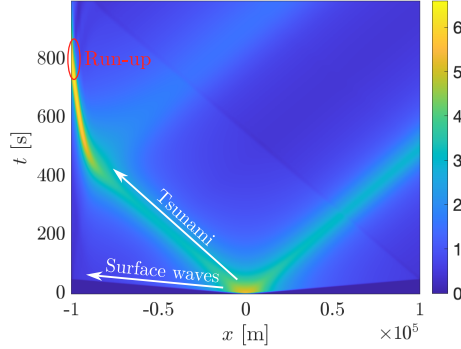
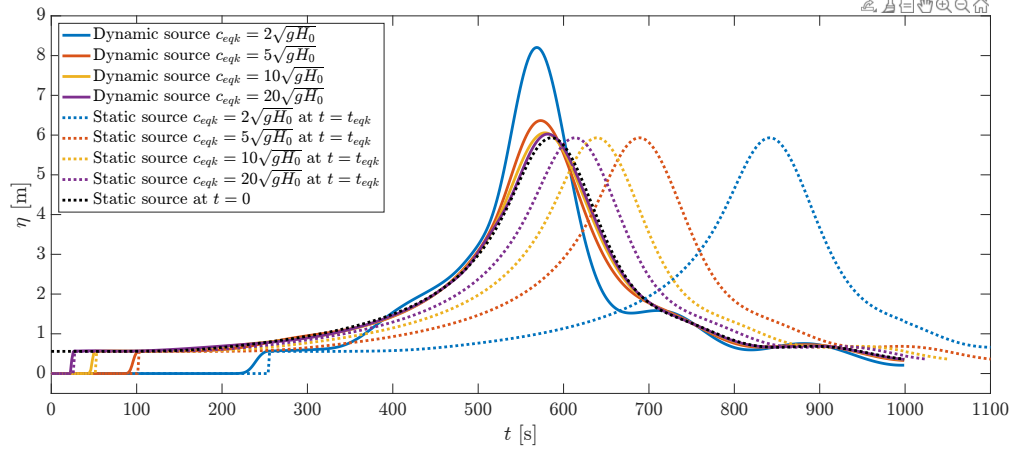
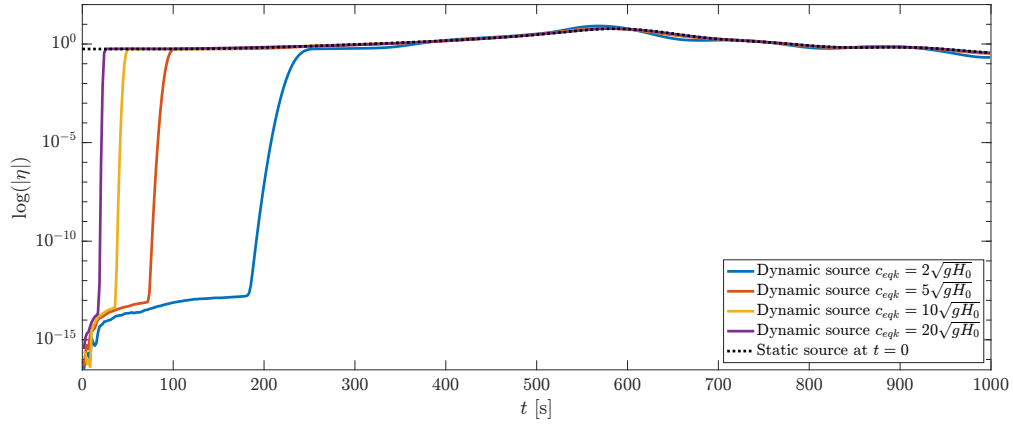


Figure 24: *1D earthquake-induced tsunamigenesis*. The complete space-time evolution of the absolute value of the free surface displacement η corresponding to the dynamic earthquake source of speed $c_{\text{eqk}} = 10\sqrt{gH_0}$.

$\eta(x_{\min}, t)$ for varying earthquake speeds $n = c_{\text{eqk}}/\sqrt{gH_0} \in \{2, 5, 10, 20\}$ near the left boundary at a location corresponding to $x = -95$ km (indicated as "run-up" in the bottom right panel of Figure 23). It is notable here that no numerical tuning is necessary to achieve such results (all employ the same spatial discretization and CFL constant) and that the longest computational time (corresponding to $n = 20$) is around two seconds. The curves illustrate the influence of the earthquake source speed c_{eqk} on the displacement found at the highest point of the beach (left boundary), demonstrating that, when considering the full dynamics of the



(a) Water height at $x = -95$ km ;



(b) Log-scale water height at $x = -95$ km.

Figure 25: *1D earthquake-induced tsunamigenesis*. Time evolution of the free surface displacement $\eta(x, t)$ at the coastline for both time-dependent and classical static (instantaneous) seafloor perturbations at different sourcing earthquake propagation speeds. The final vertical displacement of the static sources are applied at $t = 0$ or at $t = t_{eqk}$ (the final time of the corresponding earthquake motions, see Remark 6.1).

ground motion ("dynamic source"), larger water heights are observed for slower earthquakes. Additionally presented is the water elevation corresponding to the classical "static source" model associated with each earthquake speed. The static source is conventionally invoked as an instantaneous displacement representing the final or total displacement of the earthquake. One can observe that the higher the earthquake propagation speed, the better the approximation of the static source (i.e., instantaneous displacement). However, as the earthquake source speed becomes more comparable to the characteristic propagation speed of tsunami waves ($\sqrt{gH_0}$, where H_0 is the maximum depth), the static source response leads to considerable underestimation of the water elevation at the coastline. This is quantified for each case in Table 4, where one can observe that amplitude differences can be up to around 30% for the slowest earthquake speed.

The static sources in Figure 25a additionally overestimate the arrival times of their respective peaks in comparison to their corresponding dynamic source models (such differences become significantly more pronounced for slower earthquakes). This is in agreement with what has been similarly observed elsewhere [5] and is expected since such static models apply their instantaneous displacements at the end-time of the

Tsunami height		
c_{eqk}	Dynamic source	Static source
$2\sqrt{gH_0}$	8.20 m	5.93 m (−27.7%)
$5\sqrt{gH_0}$	6.37 m	5.93 m (−06.8%)
$10\sqrt{gH_0}$	6.06 m	5.93 m (−02.1%)
$20\sqrt{gH_0}$	6.03 m	5.93 m (−01.6%)

Table 4: *1D earthquake-induced tsunamigenesis*. Simulated tsunami amplitudes at coastline $x = -95$ km produced by the FC-based solver employing both the time-dependent behavior of the ground source as well as the classical static (instantaneous) source. The tsunami height underestimation due to the latter is indicated in parenthesis (%).

Tsunami arrival time			
c_{eqk}	Dynamic source	Static source at $t = 0$	Static source at $t = t_{\text{eqk}}$
$2\sqrt{gH_0}$	568.1 s	585.3 s (+17.2 s)	837.7 s (+269.6 s)
$5\sqrt{gH_0}$	573.3 s	585.3 s (+12.0 s)	686.3 s (+113.0 s)
$10\sqrt{gH_0}$	578.4 s	585.3 s (+06.9 s)	635.8 s (+057.4 s)
$20\sqrt{gH_0}$	581.9 s	585.3 s (+03.4 s)	610.5 s (+028.6 s)

Table 5: *1D earthquake-induced tsunamigenesis*. Simulated arrival times at coastline $x = -95$ km produced by the FC-based solver employing both the time-dependent behavior of the ground source as well as the classical static (instantaneous) source applied at $t = 0$ and at the end of the ground motion at $t = t_{\text{eqk}}$ (see Remark 6.1). The tsunami arrival time differences for static sourcing with respect to dynamic sourcing are indicated in parenthesis.

earthquake. Such a time must be given as an input, which may be difficult to determine; no such input is required for a dynamic source. It is notable here (and also presented in Figure 25a) that even in an overly-conservative scenario, where the static source is applied as an initial condition of the water elevation at $t = 0$ (at the beginning of the earthquake instead of at the end), such a delay (purely due to neglecting the dynamics) is still observable when compared to the dynamic source results for slower earthquakes. To the best of the author’s knowledge, the delay and its implications as a function of earthquake speed have not been explicitly demonstrated before in a parameter study for such configurations (strike-slip ruptures have been studied only recently [5, 6]). Indeed, a quantification of arrival times in Table 5 shows that the discrepancy in arrival times is at least 25 seconds for the fastest earthquake speed considered and can be more than four minutes for the slowest when the static displacement is applied at $t = t_{\text{eqk}}$. Even for a conservative $t = 0$, the overestimation can still be observed.

Figure 25b presents the same water surface heights in a log-axis at the same left boundary, revealing the arrivals of the rupture waves and the initial uplift of the water. These possibly-measurable low amplitude signals in dynamic water elevations may be valuable for tsunami forecasting. Indeed, ongoing work entails full parametric studies in order to establish correlations between such signatures and the ultimate timing/amplitude of the resulting primary tsunami waves.

6.2. 2D formulation

The problem configuration in 1D can be extended to 2D with a similar time-dependent seafloor displacement, inspired by realistic scenarios, given by

$$\xi(x, y, t) = \int_0^t \xi_t(x, y, \tau) d\tau, \quad (54)$$

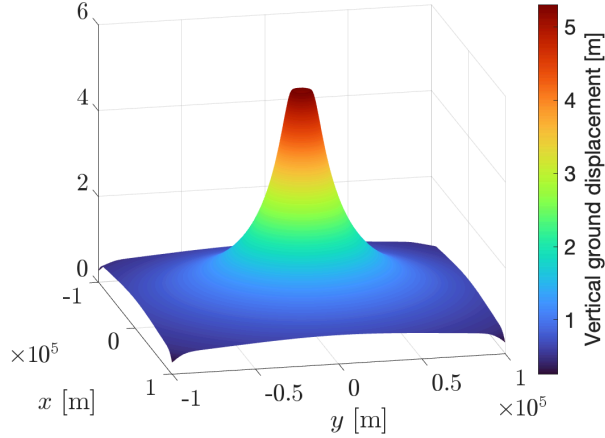


Figure 26: *2D earthquake-induced tsunamigenesis*. The final 2D ground displacement for the source $\xi(x, y, t)$ corresponding to Eq. (54).

where ξ_t is the time-derivative of the vertical displacement (i.e., vertical seafloor velocity) given by

$$\xi_t(x, y, t) = \frac{nA}{\sqrt{(r/L)^2 + \varepsilon^2}} \exp\left(-\frac{(r - c_{\text{eqk}}t)^2}{2\sigma^2}\right) \quad (55)$$

for radial distance $r = \sqrt{x^2 + y^2}$, an amplitude scaling $A = 1.67 \times 10^{-1}$ m/s, a unitless regularization parameter $\varepsilon = 0.5$, pulse width $\sigma = 4.24$ km, and a decay parameter $L = 20$ km. The final 2D displacement is illustrated in Figure 26.

Over a similarly-sized domain $x, y \in [-100, 100]$ km, the initial (unperturbed) bathymetry is that of a hyperbolic tangent beach similar to Section 6.1, similarly given by $h_0(x, y) = H_0 - s(x, y)$ for maximum depth $H_0 = 4$ km, where the initial seafloor topography $s(x, y)$ given by

$$s(x, y) = \frac{S}{2} (1 - \tanh(a(x - x_1))) (x_1 - x) \quad (56)$$

for $x_1 = -85$ km, $a = 2 \times 10^{-4} \text{ m}^{-1}$ and $S = 3.99$ km. The initial condition corresponds to that of still water (i.e. $\eta(x, y, 0) = 0$, $u(x, y, 0) = 0$ and $v(x, y, 0) = 0$), and the boundary conditions are prescribed as non-reflecting (see Eq. (9)). All simulations that follow employ $N_x = N_y = 300$ discretization points, up to a final time $t_{\text{max}} = 1000$ s. Figure 27 presents snapshots at various times, produced by the FC-based solver, of the tsunami propagation and its ground motion source corresponding to an example earthquake speed of $c_{\text{eqk}} = 10\sqrt{gH_0}$. As illustrated in the figures, earthquake surface waves propagate on the sea floor, leading to a corresponding uplift of water height of the same value due to the non-compressibility hypothesis (Figure 27b). The ground motion source propagates at $c_{\text{eqk}} = 10\sqrt{gH_0}$ (Figure 27c) until its waves reach the domain boundaries (Figure 27d). Meanwhile the corresponding tsunami wave propagates at a longer time-scale (Figure 27e) until the maximal wave height is achieved near the coastline (Figure 27f).

Similarly to the previous 1D formulation, the importance of considering earthquake dynamics in 2D is demonstrated in Figure 28a, where the time evolution of water elevation $\eta(x_{\text{min}}, t)$ is measured for varying earthquake speeds $n = c_{\text{eqk}}/\sqrt{gH_0} \in \{2, 5, 10, 20\}$ near the left boundary at a location corresponding to $x = -95$ km and $y = 0$ km (indicated as "run-up" in Figure 27f). The conclusions drawn for the 1D case remain valid for the 2D model: employing time-dependent seafloor motion, larger tsunami heights

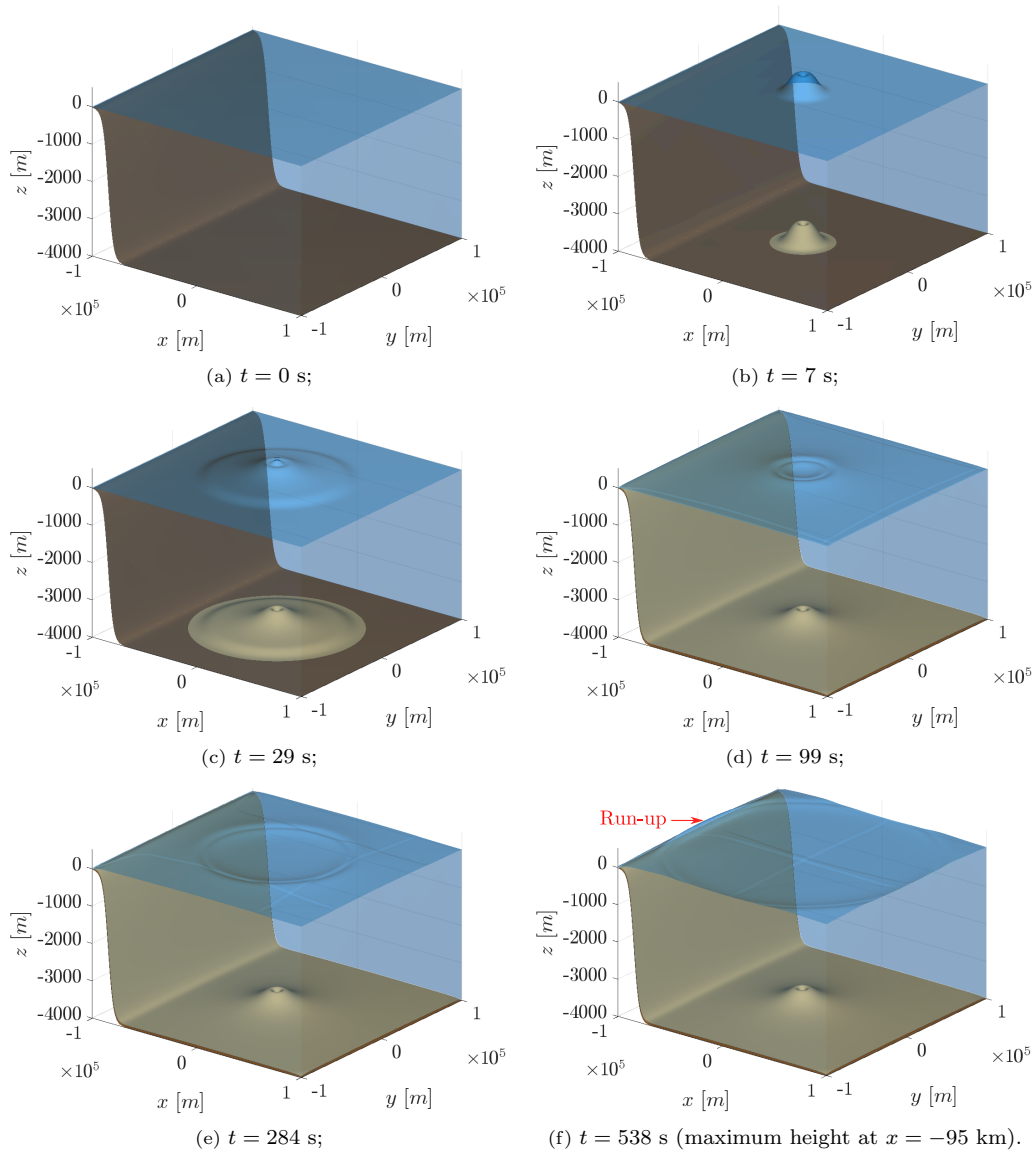
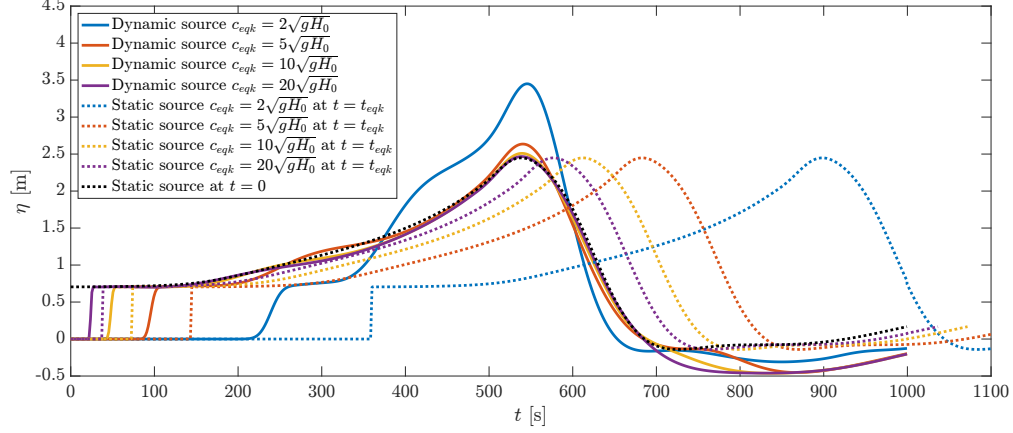
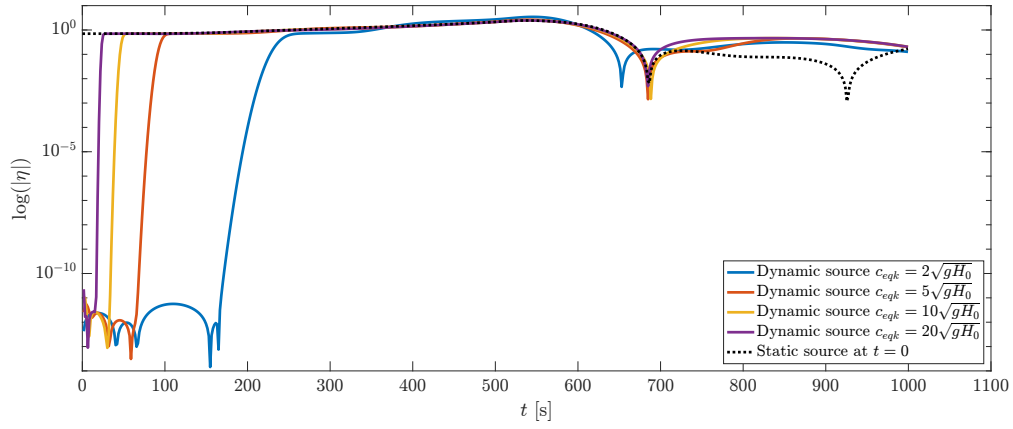


Figure 27: *2D earthquake-induced tsunamigenesis*. Snapshots at various times of tsunami generation and propagation, including the dynamic earthquake source of speed $c_{\text{eqk}} = 10\sqrt{gH_0}$. The free surface displacement (blue) and the ground perturbation (yellow) are amplified for visualization ($\times 100$).

correspond to slower earthquakes. The "static source" models presented for each earthquake speed highlight the underestimation of the tsunami height and arrival time when employing such classical instantaneous displacements. These observations are quantified for each case in [Table 6](#) and [Table 7](#), which additionally present the differences in water heights and the differences in arrival times, respectively. Additionally, including in the 1D case, the FC-based solver is able to produce all solutions with very low computational cost: all 2D simulations are produced in under 44 seconds in MATLAB (without MEX files). Indeed, the computational times for all the 1D and 2D simulations of this section, presented in [Table 8](#), imply strong potential for real-time or early warning risk assessments (with no added cost for considering time-dependent sources).



(a) Water height at $(x = -95, y = 0)$ km;



(b) Log-scale water height at $(x = -95, y = 0)$ km.

Figure 28: *2D earthquake-induced tsunamigenesis*. Time evolution of the free surface $\eta(x, y, t)$ at the left domain edge (run-up) $(x, y) = (-95, 0)$ km for both time-dependent and classical static (instantaneous) seafloor perturbations at different sourcing earthquake propagation speeds. The final vertical displacement of the static sources are applied at $t = 0$ or at $t = t_{eqk}$ (the final time of the corresponding earthquake motions, see Remark 6.1).

Tsunami height		
c_{eqk}	Dynamic source	Static source
$2\sqrt{gH_0}$	3.45 m	2.45 m (−29.0%)
$5\sqrt{gH_0}$	2.64 m	2.45 m (−07.1%)
$10\sqrt{gH_0}$	2.51 m	2.45 m (−02.4%)
$20\sqrt{gH_0}$	2.47 m	2.45 m (−00.7%)

Table 6: *2D earthquake-induced tsunamigenesis*. Simulated tsunami amplitudes at coastline $(x, y) = (-95, 0)$ km produced by the FC-based solver employing both the time-dependent behavior of the ground source as well as the classical static (instantaneous) source. The tsunami height underestimation due to the latter is indicated in parenthesis (%).

For the 2D case presented here, Figure 29 presents the time evolution of the water height at different values (locations) of y on the coastline $x = -95$ km (denoted as simulated "stations" which can correspond in practice to, e.g., DART buoys). The arrival times are expectedly delayed in relation to $y = 0$ due to the radial nature of the 2D tsunami waves. Even at other locations, the classical static source model leads to an underestimation of tsunami height and an overestimation of the tsunami arrival time. Such results the efficacy of the FC-based solver in treating problems where complex earthquake ground sources are imposed

Tsunami arrival time			
c_{eqk}	Dynamic source	Static source at $t = 0$	Static source at $t = t_{\text{eqk}}$
$2\sqrt{gH_0}$	545.2 s	538.5 s (−6.7 s)	895.4 s (+350.2 s)
$5\sqrt{gH_0}$	540.2 s	538.5 s (−1.7 s)	681.3 s (+141.1 s)
$10\sqrt{gH_0}$	538.5 s	538.5 s (+0.0 s)	609.9 s (+071.4 s)
$20\sqrt{gH_0}$	538.5 s	538.5 s (+0.0 s)	574.2 s (+035.7 s)

Table 7: *2D earthquake-induced tsunamigenesis*. Simulated arrival times at coastline $(x, y) = (-95, 0)$ km produced by the FC-based solver employing both the time-dependent behavior of the ground source as well as the classical static (instantaneous) source applied at $t = 0$ and at the end of the ground motion at $t = t_{\text{eqk}}$ (see Remark 6.1). The tsunami arrival time differences for static sourcing with respect to dynamic sourcing are indicated in parenthesis.

c_{eqk}	Computation time (1D)	Computation time (2D)
static	0.20 s	41.39 s
$2\sqrt{gH_0}$	0.20 s	40.60 s
$5\sqrt{gH_0}$	0.19 s	43.78 s
$10\sqrt{gH_0}$	0.19 s	43.67 s
$20\sqrt{gH_0}$	0.19 s	39.96 s

Table 8: *2D earthquake-induced tsunamigenesis*. Computation times for the FC-based solver in producing the 1D and 2D solutions of this section (averaged over multiple runs). All simulations are conducted in MATLAB (Section 3.4).

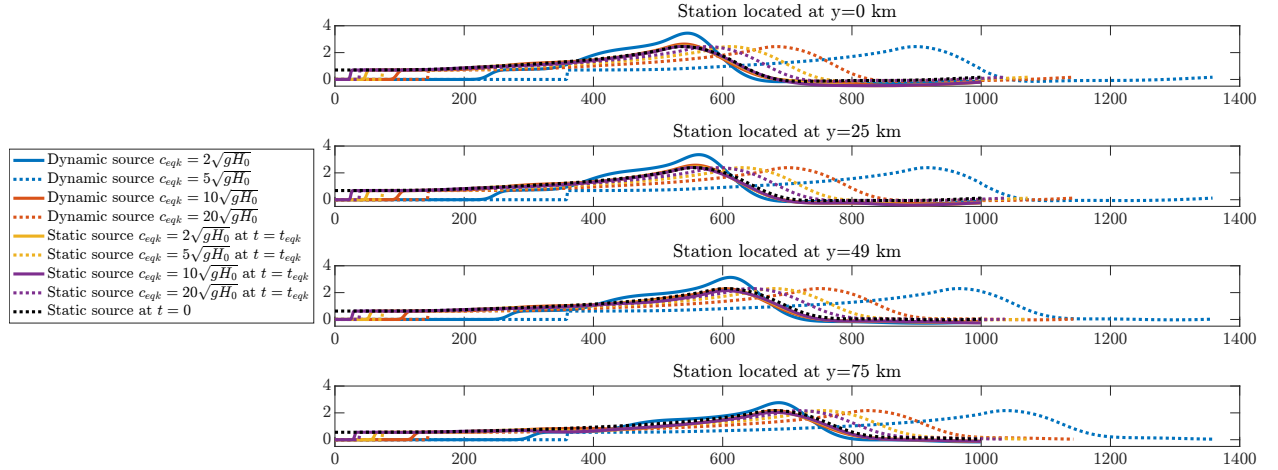


Figure 29: *2D earthquake-induced tsunamigenesis*. Time evolution of the free surface displacement $\eta(x, y, t)$ at various locations (stations) y along the coastline $x = -95$ km for both time-dependent and classical (instantaneous) seafloor perturbations at different sourcing earthquake speeds.

at the sea floor, particularly through consideration of the dynamic seafloor displacement and velocity. The authors encourage the use of the 1D and 2D formulations of the problem introduced in this section for future benchmark investigation concerning dynamic source models.

7. Conclusions

This work introduces a high-order spectral solver based on a Fourier continuation (FC) methodology for solving the nonlinear shallow water equations with dynamic seabed motion. A number of numerical experiments attest to fifth-order spatial accuracy while minimal numerical dispersion errors, making it well-suited for long-distance or high-frequency tsunami propagation modeling. Additionally, several classical and semi-classical benchmarks are provided to validate the present implementation of the solver against

analytical solutions as well as experimental data, demonstrating its capability in capturing critical physical effects relevant to tsunami generation and propagation with minimal numerical errors. A number of results are presented in comparison to other solvers, including high-order finite volume and finite difference methods, where the FC-based approach is highly competitive, accurately preserving waveforms over extended spatial and temporal scales at a much lower computational cost than other considered solvers. Furthermore, a new problem configuration, inspired by realistic ground motion settings, is proposed and highlights the relevance of considering dynamic ground motion in tsunami modeling and the efficacy of employing an FC-based approach in such contexts. This includes a preliminary parametric study (a first, to the best of the author’s knowledge) of the effects of earthquake speed on tsunamigenesis and the subsequent wave dynamics.

The FC-based approach can be further improved by the addition of explicit shock-capturing schemes (e.g., ENO or WENO [60, 61]), although the present implementation is demonstrated in this paper to be reasonably effective without any special treatment. Future work also entails the full coupling of the solver with dynamic rupture models and global-scale bathymetric datasets. Additionally, the applicability of the solver in operational tsunami warning systems can be enhanced by incorporating curvilinear mesh generation strategies, which facilitate adaptive meshing as well as treatment of more complex and realistic geometries [21]. The latter may involve more large-scale configurations that require optimization of the solver for high-performance computing (HPC) architectures, such as those with GPU acceleration (the computational complexity here being dominated by the FFT).

Recent contributions [5, 6] have demonstrated the importance of considering dynamic seafloor motion (in terms of time-dependent displacement and velocity) in the generation of tsunamis due to strike-slip earthquakes. The results of Section 6 extend this idea and imply the importance in capturing the interplay of earthquake dynamics and tsunami propagation even for subduction earthquakes (which are conventionally modeled as instantaneous seafloor displacements). The parameter studies presented herein suggest that such considerations are particularly relevant when the speed of the ground surface waves are comparable to the characteristic wavespeed of the resulting tsunami waves, revealing an unexplored potential for improving tsunami hazard assessment. The robust and efficient nature of the proposed FC solver, in terms of considering such motions with minimal tuning of numerical parameters, can be highly beneficial for early warning systems and for real-time forecasting, including for the training of physics-based machine learning surrogate models [62] with physically-faithful simulated data.

Acknowledgments

T.M., H.S.B., F.A.: this project has received financial support from the CNRS through the MITI interdisciplinary programs. H.S.B.: acknowledges additional support from the European Research Council (ERC) PERSISMO, Grant 865411. F.A.: acknowledges additional support from the Agence Nationale de la Recherche (ANR), Grant ANR-23-CE46-0008. The authors are grateful to Prof A.E. Elbanna and Dr M. Abdelmeguid for sharing some experimental data, and to Prof M. Derakhti for valuable discussions concerning the benchmark considered in Section 5.5.

References

- [1] F. Imamura, S. P. Boret, A. Suppasri, A. Muhari, Recent occurrences of serious tsunami damage and the future challenges of tsunami disaster risk reduction, *Progress in Disaster Science* 1 (2019) 100009.

- [2] Z. Kowalik, W. Knight, T. Logan, P. Whitmore, The tsunami of 26 december, 2004: Numerical modeling and energy considerations, *Pure and Applied Geophysics* 164 (2007) 379–393.
- [3] D. Sugawara, Numerical modeling of tsunami: advances and future challenges after the 2011 tohoku earthquake and tsunami, *Earth-Science Reviews* 214 (2021) 103498.
- [4] M. Hajihassanpour, B. Bonev, J. S. Hesthaven, A comparative study of earthquake source models in high-order accurate tsunami simulations, *Ocean Modelling* 141 (2019) 101429.
- [5] F. Amlani, H. S. Bhat, W. J. F. Simons, A. Schubnel, C. Vigny, A. J. Rosakis, J. Efendi, A. E. Elbanna, P. Dubernet, H. Z. Abidin, Supershear shock front contribution to the tsunami from the 2018 Mw 7.5 Palu, Indonesia earthquake, *Geophysical Journal International* 230 (3) (2022) 2089–2097.
- [6] A. Elbanna, M. Abdelmeguid, X. Ma, F. Amlani, H. S. Bhat, C. Synolakis, A. J. Rosakis, Anatomy of strike-slip fault tsunami genesis, *Proceedings of the National Academy of Sciences* 118 (19) (2021) e2025632118.
- [7] D. Dutykh, D. Clamond, Modified shallow water equations for significantly varying seabeds, *Applied mathematical modelling* 40 (23-24) (2016) 9767–9787.
- [8] F. Imamura, A. C. Yalciner, G. Ozyurt, [Tsunami modelling manual \(TUNAMI model\)](#) (1995).
URL https://www.tsunami.irides.tohoku.ac.jp/media/files/_u/project/manual-ver-3_1.pdf
- [9] R. J. LeVeque, D. L. George, M. J. Berger, Tsunami modelling with adaptively refined finite volume methods, *Acta Numerica* 20 (2011) 211–289.
- [10] O. Delestre, F. Darboux, F. James, C. Lucas, C. Laguerre, S. Cordier, FullSWOF: A free software package for the simulation of shallow water flows, Research report, Mapmo, université d’Orléans ; Institut National de la Recherche Agronomique, 38 pages (Jan. 2014).
- [11] J. Zhou, A lattice boltzmann model for the shallow water equations, *Computer Methods in Applied Mechanics and Engineering* 191 (32) (2002) 3527–3539.
- [12] R. A. R. Roselli, G. Vernengo, S. Brizzolara, R. Guercio, Sph simulation of periodic wave breaking in the surf zone - a detailed fluid dynamic validation, *Ocean Engineering* 176 (2019) 20–30.
- [13] Z. Wei, R. A. Dalrymple, A. Hérault, G. Bilotta, E. Rustico, H. Yeh, Sph modeling of dynamic impact of tsunami bore on bridge piers, *Coastal Engineering* 104 (2015) 26–42.
- [14] T. Utnes, A finite element solution of the shallow-water wave equations, *Applied Mathematical Modelling* 14 (1) (1990) 20–29.
- [15] A. Zaytsev, A. Kurkin, E. Pelinovsky, A. C. Yalciner, Numerical tsunami model nami-dance., *Science of Tsunami Hazards* 38 (4) (2019).
- [16] P. Heinrich, A. Jamelot, A. Cauquis, A. Gailler, Taitoko, an advanced code for tsunami propagation, developed at the french tsunami warning centers, *European Journal of Mechanics - B/Fluids* 88 (2021) 72–88.

- [17] D. Durran, Numerical Methods for Wave Equations in Geophysical Fluid Dynamics, Texts in Applied Mathematics, ISSN 0939-2475, Springer New York, NY, 1999.
- [18] A. Deraemaeker, I. Babuška, P. Bouillard, Dispersion and pollution of the FEM solution for the Helmholtz equation in one, two and three dimensions, *International journal for numerical methods in engineering* 46 (4) (1999) 471–499.
- [19] I. Aida, Numerical computation of a tsunami based on a fault origin model of an earthquake, *Journal of Japan Seismological Society* 27 (1974) 141–154.
- [20] S. Marras, K. T. Mandli, Modeling and simulation of tsunami impact: a short review of recent advances and future challenges, *Geosciences* 11 (1) (2020) 5.
- [21] F. Amlani, O. P. Bruno, An FC-based spectral solver for elastodynamic problems in general three-dimensional domains, *Journal of Computational Physics* 307 (2016) 333 – 354.
- [22] O. P. Bruno, M. Lyon, High-order unconditionally stable FC-AD solvers for general smooth domains i. Basic elements, *Journal of Computational Physics* 229 (6) (2010) 2009–2033.
- [23] F. Amlani, N. Pahlevan, A stable high-order FC-based methodology for hemodynamic wave propagation, *Journal of Computational Physics* 405 (2020) 109130.
- [24] O. P. Bruno, D. V. Leibovici, General-domain FC-based shock-dynamics solver i: Basic elements, *arXiv preprint arXiv:2506.16076* (2025).
- [25] E. L. Gaggioli, O. P. Bruno, D. M. Mitnik, Light transport with the equation of radiative transfer: the Fourier Continuation–Discrete Ordinates (FC–DOM) Method, *Journal of Quantitative Spectroscopy and Radiative Transfer* 236 (2019) 106589.
- [26] M. Fontana, O. P. Bruno, P. D. Mininni, P. Dmitruk, Fourier continuation method for incompressible fluids with boundaries, *Computer Physics Communications* 256 (2020) 107482.
- [27] O. P. Bruno, J. Paul, Two-dimensional fourier continuation and applications, *SIAM Journal on Scientific Computing* 44 (2) (2022) A964–A992.
- [28] N. Albin, O. P. Bruno, A spectral FC solver for the compressible Navier–Stokes equations in general domains I: Explicit time-stepping, *Journal of Computational Physics* 230 (16) (2011) 6248–6270.
- [29] F. Amlani, H. Wei, N. M. Pahlevan, A Fourier-based methodology without numerical diffusion for conducting dye simulations and particle residence time calculations, *Journal of Computational Physics* 493 (2023) 112472.
- [30] F. Amlani, N. M. Pahlevan, A high-order space-time Fourier continuation approach for one-dimensional hemodynamics and wave propagation in the entire human circulatory system, *Physics of Fluids* 37 (7) (2025).
- [31] A. Aghilinejad, F. Amlani, M. Gharib, Power-frequency relationship of wave dynamics in fluid-filled compliant tubes, *Physical Review Fluids* 10 (3) (2025) 033102.

- [32] C. Bilgi, F. Amlani, H. Wei, N. Rizzi, N. M. Pahlevan, Thermal and postural effects on fluid mixing and irrigation patterns for intraventricular hemorrhage treatment, *Annals of Biomedical Engineering* 51 (6) (2023) 1270–1283.
- [33] X. Wang, P. L.-F. Liu, An analysis of 2004 sumatra earthquake fault plane mechanisms and indian ocean tsunami, *Journal of Hydraulic Research* 44 (2) (2006) 147–154.
- [34] L. S. Abrahams, L. Krenz, E. M. Dunham, A.-A. Gabriel, T. Saito, Comparison of methods for coupled earthquake and tsunami modelling, *Geophysical Journal International* 234 (1) (2023) 404–426.
- [35] B. De St Venant, Théorie du mouvement non permanent des eaux, avec application aux crues des rivières et à l'introduction de marées dans leurs lits, *Comptes rendus hebdomadaires des séances de l'Académie des sciences* 73 (99) (1871) 148–154.
- [36] A. Kundu, *Tsunami and nonlinear waves*, Vol. 316, Springer, 2007.
- [37] D. Dutykh, *Mathematical modelling of tsunami waves*, Ph.D. thesis, École normale supérieure de Cachan-ENS Cachan (2007).
- [38] R. Setiyowati, Sumardi, A simulation of shallow water wave equation using finite volume method: Lax-friedrichs scheme, *Journal of Physics: Conference Series* 1306 (1) (2019) 012022.
- [39] D. Dutykh, D. Mitsotakis, X. Gardeil, F. Dias, On the use of the finite fault solution for tsunami generation problems, *Theoretical and Computational Fluid Dynamics* 27 (2013) 177–199.
- [40] M.-O. Bristeau, B. Coussin, *Boundary conditions for the shallow water equations solved by kinetic schemes*, Ph.D. thesis, INRIA (2001).
- [41] A. Delis, T. Katsaounis, Numerical solution of the two-dimensional shallow water equations by the application of relaxation methods, *Applied Mathematical Modelling* 29 (8) (2005) 754–783.
- [42] Y. Wei, X.-Z. Mao, K. F. Cheung, Well-balanced finite-volume model for long-wave runoff, *Journal of Waterway, Port, Coastal, and Ocean Engineering* 132 (2) (2006) 114–124.
- [43] F. Dias, D. Dutykh, Dynamics of tsunami waves, in: *Extreme man-made and natural hazards in dynamics of structures*, Springer, 2007, pp. 201–224.
- [44] C. Van Loan, *Computational frameworks for the fast Fourier transform*, SIAM, 1992.
- [45] J.-P. Demailly, *Analyse numérique et équations différentielles.*, Collection Grenoble sciences, ISSN 0767-371X, Les Ulis - EDP Sciences, 2016.
- [46] J. Hesthaven, R. Kirby, Filtering in legendre spectral methods, *Mathematics of Computation* 77 (263) (2008) 1425–1452.
- [47] P. J. Roache, Code Verification by the Method of Manufactured Solutions , *Journal of Fluids Engineering* 124 (1) (2001) 4–10.
- [48] R. P. Fedkiw, T. Aslam, B. Merriman, S. Osher, A non-oscillatory eulerian approach to interfaces in multimaterial flows (the ghost fluid method), *Journal of computational physics* 152 (2) (1999) 457–492.

- [49] L. Lundgren, K. Mattsson, An efficient finite difference method for the shallow water equations, *Journal of Computational physics* 422 (2020) 109784.
- [50] V. Michel-Dansac, C. Berthon, S. Clain, F. Foucher, A well-balanced scheme for the shallow-water equations with topography, *Computers & Mathematics with Applications* 72 (3) (2016) 568–593.
- [51] M. Ricchiuto, R. Abgrall, H. Deconinck, Application of conservative residual distribution schemes to the solution of the shallow water equations on unstructured meshes, *Journal of Computational Physics* 222 (1) (2007) 287–331.
- [52] R. J. LeVeque, Balancing source terms and flux gradients in high-resolution godunov methods: the quasi-steady wave-propagation algorithm, *Journal of computational physics* 146 (1) (1998) 346–365.
- [53] C. E. Synolakis, E. N. Bernard, V. V. Titov, U. Kânoglu, F. I. Gonzalez, Validation and Verification of Tsunami Numerical Models, *Pure and Applied Geophysics* 165 (2008) 2197–2228.
- [54] C. Synolakis, Standards, criteria, and procedures for noaa evaluation of tsunami numerical models, NOAA Technical Memorandum OAR PMEL-135 (2007).
- [55] U. Kânoglu, V. Titov, B. Aydin, C. Moore, T. Stefanakis, H. Zhou, M. Spillane, C. Synolakis, Focusing of long waves with finite crest over constant depth, *Proc R Soc A* 469 (2013).
- [56] IAEA, Benchmark Analysis of Numerical Models for Tsunami Simulation, no. 1973 in TECDOC Series, International Atomic Energy Agency, Vienna, 2022.
- [57] T. Baba, N. Takahashi, Y. Kaneda, K. Ando, D. Matsuoka, T. Kato, Parallel implementation of dispersive tsunami wave modeling with a nesting algorithm for the 2011 tohoku tsunami, *Pure Appl. Geophys.* 172 (2015) 3455–3472.
- [58] M. Derakhti, R. A. Dalrymple, E. A. Okal, C. E. Synolakis, Temporal and topographic source effects on tsunami generation, *Journal of Geophysical Research: Oceans* 124 (2019) 5270–5288.
- [59] J. L. Hammack, A note on tsunamis: their generation and propagation in an ocean of uniform depth, *Journal of Fluid Mechanics* 60 (4) (1973) 769–799.
- [60] C.-W. Shu, Essentially non-oscillatory and weighted essentially non-oscillatory schemes for hyperbolic conservation laws, in: *Advanced Numerical Approximation of Nonlinear Hyperbolic Equations: Lectures given at the 2nd Session of the Centro Internazionale Matematico Estivo (CIME) held in Cetraro, Italy, June 23–28, 1997*, Springer, 2006, pp. 325–432.
- [61] K. Shahbazi, N. Albin, O. P. Bruno, J. S. Hesthaven, Multi-domain fourier-continuation/weno hybrid solver for conservation laws, *Journal of Computational Physics* 230 (24) (2011) 8779–8796.
- [62] P. Andraud, A. Gailler, T. Sprunck, N. Vayatis, Deep learning models exploration for rapid forecasting of coastal tsunami impact in near field context – application to the French Mediterranean coastline, *EGU General Assembly 2022, Vienna, Austria, EGU22-12716* (2022).